

2013

Characterization of ricinoleic acid coated spinel nanoparticles and microfabrication of a four point device for nanowire electronic conductivity measurement

<https://hdl.handle.net/2144/12118>

Downloaded from DSpace Repository, DSpace Institution's institutional repository

BOSTON UNIVERSITY
COLLEGE OF ENGINEERING

Thesis

**CHARACTERIZATION OF RICINOLEIC ACID COATED SPINEL
NANOPARTICLES
AND
MICROFABRICATION OF A FOUR POINT DEVICE FOR NANOWIRE
ELECTRONIC CONDUCTIVITY MEASUREMENT**

by

ANNY MINERVA HIERRO

B.S., College of Saint Elizabeth, 2010

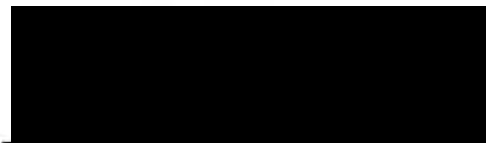
Submitted in partial fulfillment of the
requirements for the degree of
Master of Science

2013

© 2013 by
Anny Minerva Hierro
All rights reserved

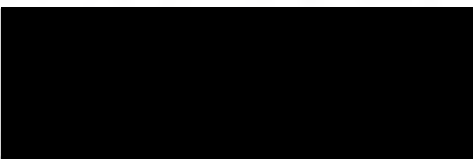
Approved by

First Reader



Linda H. Doerrer, Ph.D.
Associate Professor of Chemistry

Second Reader



Xin Zhang, Ph.D.
Professor, Department of Mechanical Engineering

Acknowledgements

I have been faced with many difficult choices in my life. Graduate school was, honestly, one of them. Leaving my family and stepping outside my comfort zone was challenging. However, those encouraging me provided the confidence and support I needed both intellectually and emotionally. I knew from the start that this path would be impossible if approached alone and it is thanks to the wonderful group of people that pushed me along the way that I was able to complete this crucial stage in my education.

I would first like to give special thanks to Prof. Linda H. Doerrer, not only for warmly welcoming me to her group, but for taking her role as mentor seriously, teaching me patiently how to be a better scientist, student, and mentor as well. Linda's enthusiasm is contagious and this passion will stay with me forever. Along with Linda, the Doerrer group has become my extended family. What started, as a group of strangers are now great friends I can confide in. Our interactions in and outside of lab made me feel welcomed and comfortable and their help allowed me to grow. I am thankful for sharing this experience with you all.

Beyond the lab, out of the state, and back in New Jersey resides a very special group of people, my favorite group of people, my family. My parents Maria M. Guzman and Bartolo M. Hierro, came from humble beginnings and have done everything in their power to mold me into the person I am today. From a young age I was encouraged to pursue my dreams and to never limit myself. I

am a confident individual because they believed in my capabilities. Their love, tenderness and trust are the greatest gift a daughter can ask for and I would like to take this opportunity to finally say thank you, I love you both more than you know.

My siblings, Anel Hierro (Cosi) and Enmanuel Hierro (Betty), my best friends and partners in crime. You both play an important role in my life; my protective older brother taught me how to ask for help and how to choose the right people to welcome into my life. My talented younger sister, taught me to care for others, to be a leader, to challenge the world and to always be myself. The love I feel for you two cannot be easily explained, but I know you both know what I mean, thank you for choosing me as a friend and loving me the way I am.

At last my loving Boyfriend Luis A. Cruz, the sacrifices he has made for the sake of my education have been many, accepting my decision of moving and putting his needs to a side to help me forward was too much for me to ask, but he did it gladly. My late nights studying became his, as well as making sure I was fed and our home clean. All the times I was afraid I was going to fail he was there to hold my hand. Babe, I know this has been tough on you too, but thank you for making it fun as well and reminding me not to lose myself in the process, I love you.

My experience at Boston University was remarkable and it is thanks to those around me as well as my classmates, colleagues and everyone at the

Material Science and Engineering division (MSE) who have supported me along the way. Thank you for your help and support.

**CHARACTERIZATION OF RICINOLEIC ACID COATED SPINEL
NANOPARTICLES
AND
MICROFABRICATION OF A FOUR POINT DEVICE FOR NANOWIRE
ELECTRONIC CONDUCTIVITY MEASUREMENT**

ANNY MINERVA HIERRO

ABSTRACT

I. Characterization of Ricinoleic Acid Coated Spinel Nanoparticles

Magnetic nanoparticles are of great interest today due to their potential contributions to the development of new imaging technologies. Ferrites, in particular, stand out because of their significant magnetic susceptibilities and relative chemical stability as candidates for a number of applications in technological, biomedical and environmental research. In this chapter, the vibrating magnetic susceptibility studies of a series of ricinoleic acid coated non-magnetite spinels with the form MFe_2O_4 ($M = Co, Ni, Mn, Zn$) will be presented. Results indicate similarities between the magnetic saturation susceptibility (M_s) values obtained for Ni and Mn samples (55.9 emu/g and 48.8 emu/g, respectively), and published values for spinel nanoparticles coated with oleic acid and other surfactants (~50 emu/g and ~20-50 emu/g respectively)^[1]. Co samples

demonstrated a low M_S of 5.06 emu/g in comparison to published results (~6-90 emu/g^[1b, 2]). These results can be attributed to small core size^[2a] and/or presence of other species during measurements such as cobalt oxide^[3]. Finally, the Zn sample demonstrated dispersion difficulties and low magnetic susceptibility and was subjected to a series of pH dependent studies resulting in a maximum M_S of 17.7 emu/g at pH 8. Maximum magnetic susceptibilities have been attained by optimization of facile air-stable hybrid co-precipitation hydrothermal syntheses demonstrating how magnetic susceptibilities can be affected by the reaction conditions, which affect the size of nanoparticles.

II. Microfabrication of a Four Point Device for Nanowire Electronic Conductivity Measurement

The development of one-dimensional (1D), electronically conducting nanowires has attracted interest due to their possible integration into submicroscale electronic devices. The Doerrer group is investigating the preparation of electrically conductive, 1D, one atom wide nanowires employing a bottom-up approach. This chapter describes the design and development of a substrate for four-point probe electronic conductivity measurements with sub-micrometer scale Au wires utilizing micro-fabrication techniques for the characterization of the aforementioned structures. Potentially, the design would allow the user to deposit a sample on the micrometer scale Au contacts without

the need for submicron probes. Initial devices are not well defined at the smallest submicron features ($<1 \mu\text{m}$). Preliminary thin film four point probe measurements of TTF-TCNQ (tetrathiafulvalene tetracyanoquinodimethane) using dropcast films on submillimeter features are encouraging.

Table of Content

Chapter 1	1
1.0. Introduction	2
1.1. Nanomaterials	4
1.1.1. Nanoparticles	4
1.2. Magnetic Nanoparticles	4
1.2.1. Ferrites	4
1.2.3. Normal and Inverse Spinel	5
1.3. Preparation Methods	7
1.3.1. Biological Methods	7
1.3.1.1. Biomolecule-Mediated Nanoparticles Self-Assembly	7
1.3.1.2 Biology Assisted Sol/Gel Process	8
1.3.2. Physical Methods	8
1.3.2.1. Ball Milling	8
1.3.2.2. Mechanical Processes of Powder Mixture	9
1.3.3. Chemical Methods	9
1.3.3.1. Co-Precipitation	10
1.3.3.2. Microemulsions	10
1.3.3.3. Sol-Gel	11
1.3.3.4. Gas/Aerosol	11
1.3.3.5. Polyol Method	12
1.3.3.6. Thermal Decomposition	12
1.3.3.7. Hydrothermal	13

2.0 Experimental	13
2.0.1. General Procedures	15
2.1. Preparation of Nanoparticles	15
2.1.1. CoFe₂O₄-RA	16
2.1.2. NiFe₂O₄-RA	17
2.1.3. MnFe₂O₄-RA	17
2.1.4. ZnFe₂O₄-RA	18
2.2. Preliminary Results	19
2.3. Synthesis Optimization- MnFe₂O₄-RA and ZnFe₂O₄-RA NPs	21
2.4. Nanoparticle Characterization	21
2.4.1. Sample Preparation	24
2.4.2. TGA General Procedures	25
2.4.3. Sample Calculations	26
2.4.4. Vibrating Sample Magnetometer	27
2.4.5. Vibrating Sample Magnetometer (VSM) Calculations	28
3.0. Results and Discussion	28
3.1. TG Analysis of CoFe₂O₄-RA, NiFe₂O₄-RA and MnFe₂O₄-RA	28
3.1.1. Cobalt Ferrite	30
3.1.2. Nickel Ferrite	31
3.1.3. Manganese Ferrite	31
3.2. VSM Analysis of CoFe₂O₄-RA, NiFe₂O₄-RA and MnFe₂O₄-RA	31
3.2.1. Cobalt Ferrite	32
3.2.2. Nickel Ferrite	33

3.2.3. Manganese Ferrite	34
3.2.4. Comparison of CoFe_2O_4 -RA, NiFe_2O_4 -RA and MnFe_2O_4 -RA M_S	35
3.3. TG analysis of ZnFe_2O_4 -RA	36
3.3.1. Zinc Ferrite	37
3.4. VSM Analysis of ZnFe_2O_4 -RA at Different pH	37
3.4.1. Zinc Ferrite	38
4.4.2. Zinc Ferrite	38
4.3.2. Structural Characterization	39
4.0. Conclusions	40
Chapter 2	42
1.0. Introduction-Motivation	43
2.0. Band Theory	48
3.0. Current Methods for Measuring Electronic Conductivity	51
4.0. Four-Point Probe Theory	53
5.0. Microfabrication Techniques	55
5.1. Surface Micromachining	56
5.2. Photolithography	57
5.2.1. Positive Photoresist	58
5.2.2. Negative Photoresist	59
6.0. General Procedures	59
6.1. Materials	60
7.0. Experimental	60
7.1. CAD	61

7.2. Optical Mask	62
7.3. Chromium Etch	63
7.4. Device Development	66
7.5. Thermal Evaporation of Wires	68
7.6. Four-Point Probe Sample Preparation	71
8.0. Results and Discussion	72
8.1. Measurements	73
8.2. Further Optimization	74
8.3. Further Development-a New Approach	77
9.0. Summary and Conclusion	78
References	79
Curriculum Vitae	85

List of Tables

1.1	pH Dependence Analysis of MnFe_2O_4 and ZnFe_2O_4 NPs	22
1.2.	Time Dependence Analysis of MnFe_2O_4 and ZnFe_2O_4 NPs	23
1.3.	VSM and DLS Data	36
2.1.	Resistivity Measurements	74

List of Figures

1.1	Dispersity and Magnetic Response of CoFe_2O_4 -RA Sample	20
1.2.	Low Dispersity and Magnetic Response of ZnFe_2O_4 -RA Sample	21
1.3	TGA Thermogram of CoFe_2O_4 -RA Sample (% Mass vs Temp)	25
1.4.	TGA Thermogram of CoFe_2O_4 -RA Sample (mg vs Temp)	27
1.5.	VSM Hysteresis Curve of CoFe_2O_4 -RA	30
1.6.	TGA Thermogram of NiFe_2O_4 -RA	31
1.7.	TGA Thermogram of MnFe_2O_4 -RA	32
1.8.	VSM Hysteresis Curve of NiFe_2O_4 -RA	34
1.9.	VSM Hysteresis Curve of MnFe_2O_4 -RA	35
1.10.	Comparative VSM Hysteresis Curves	36
1.11.	TGA Thermogram of ZnFe_2O_4 -RA	37
1.12.	VSM Hysteresis Curve of ZnFe_2O_4 -RA pH 9	38
1.13.	VSM Hysteresis Curve of ZnFe_2O_4 -RA pH 8, pH 10	39
2.1.	Structure of $[\text{MM}'(\text{tba})_4(\text{pyz})]$	47
2.2.	Proposed Design for Microfabricated Electrodes	48
2.3.	Four-point Probe System	54
2.4.	Four Point Probe Device Aligned to Instrument	55
2.5.	Mask Design With Micro Features Dimensions	62
2.6.	Detail of Developed Optical Mask	64
2.7.	Detail of Developed Optical Mask	65
2.8.	Detail of Developed Optical Mask	66
2.9.	Coated Fused Silica	67

2.10. Final Product	69
2.11. Au Wires Deposited on Fused Silica Substrate	70
2.12. Au Wires Deposited on Fused Silica Substrate	71
2.13. Illustrations of New Dimensions	75
2.14. Unsuccessful Development of Pattern	76

List of Schemes

2.1. 1D Nanowires Arrangement	45
2.2. Illustration of Lantern Unit	46
2.3. Illustrations of Band Gaps for Different Materials	49
2.4. Illustration of the Fermi Level	50
2.5. Lithography Process	58
2.6. Photoresist Pattern Resulting from Positive Photoresist	59
2.7. Photoresist Pattern Resulting from Negative Photoresist	59
2.8. Illustration of Final Device	77
2.9. Illustration of Device Introducing a Trench for Slow Evaporation	77

List of Abbreviations

RA	ricinoleic acid
DCM	dichloromethane
NPs	nanoparticles
CMOS	complementary metal oxide semiconductor
DLS	dynamic light scattering
1D	1-dimensional
S	spacing
V	volts
EDX	energy dispersive X-ray spectroscopy
I	current
Et ₂ O	diethylether
EtOH	ethanol
K	Kelvin
SL	soda lime (glass)
M	molar
Me	methyl
MeOH	methanol
mg	milligram
mL	milliliter
CAD	computer aided design
mM	millimolar
mol	mole

nm	nanometer
NMR	nuclear magnetic spectroscopy
Ph	phenyl
pyz	pyrazine
RT	room temperature
SAc	thioacetate
SEM	scanning electron microscopy
ρ	rho
tba	thiobenzoate
TEM	transmission electron microscopy
tol	toluene
emu	electromagnetic unit
emu/g	electromagnetic unit per grams
G	Gauss
VSM	vibrating sample magnetometer
TGA	thermogravimetric analysis
Ω	ohms
μL	microliters
μm	micrometers
MGS	Magnus' green salt
M_s	magnetic saturation

Chapter I. Characterization of Ricinoleic Acid Coated Spinel Nanoparticles

1.0. Introduction

Magnetic nanoparticles are promising carriers for drug targeting^[4], for enhanced contrast agents for magnetic resonance imaging ^[4a, 5] and catalysis in processes such desulfurization of natural gas ^[6], due to their small scale, biocompatibility, stable dispersion in a number of solvents and their retention of magnetic properties after modification. The nanoparticles can be tailored to bind to specific sites ideal for cancer treatments and tumor targeting, as well as drug delivery^[4a, 7]. In electronic devices ferrite spinels, as nanoparticles, are actively used in a number of devices including electric motors, amplifiers, electronic sensors, and transformers^[8]. Current research focuses on biomedical imaging and diagnosis of lesions utilizing the magnetic nanoparticles to target the affected areas. Studies reveal that these nanoparticles accumulate around tumors due to differences in tissue compositions^[4a]. Current results in the field of medicine including iron oxide nanoparticles are promising and utilizing similar technology could have a great impact for petrochemical industries by the use of their contrast agent abilities in magnetic resonant imaging during reservoir analysis.

Iron oxide nanoparticles, both Fe_2O_3 and Fe_3O_4 , have been demonstrated to be of great value because of their high magnetic susceptibilities, electrical resistivity, and chemical stability^[8-9]. A particularly intensely investigated iron oxide is magnetite, $\text{Fe(II)Fe(III)}_2\text{O}_4$, one member of the spinel family. Other ferrite spinels of the form $\text{A(II)Fe(III)}_2\text{O}_4$, are also under investigation^[10]. The ability to prepare a wide variety of ferrite spinel nanostructures, in which A is a

divalent metal in a tetrahedral environment, has opened an exciting path in a number of research fields and could have a significant impact in the fields of biological and electronic technology.

The focus of the research in this thesis is the characterization of ricinoleic acid-coated ferrite spinels. Magnetic nanoparticles of benign composition and coating with high magnetic susceptibilities, stable dispersion, and resistance to high temperatures and pH variation could be perfect candidates to be introduced into petrochemical reservoirs for detection by long-range magnetic field perturbations.

The following chapter will discuss the magnetic characterization, by vibrating sample magnetometer studies and the synthesis optimization of a series of ricinoleic acid-coated spinels of the form MFe_2O_4 (M= Co, Ni, Mn, Zn). Comparative data were sought to optimize the synthesis conditions to obtain higher magnetic susceptibility without compromising the nanoparticle size, stability or morphology.

1.1. Nanomaterials

Nanomaterials are a fast growing and crucial technology sector with product consumptions ranging from personal devices, such as portable electronics to broader fields, including medical and military development. The term "nanomaterial" refers to an array of substances with at least one dimension

under 100 nanometers and can consist of polymers, ceramics or metals^[11]. The development of nanomaterials is of particular interest due to their small size domain and their behavior in comparison to their bulk counterparts. At such diminutive scales, the properties of nanomaterials vary due to the increased relative surface area and quantum effects. The difference in surface area to volume ratio can result in greater chemical reactivity and enhancement of the material properties. Most essentially, understanding the behavior of materials at this scale is crucial in enhancing their mechanical, optical, catalytic, electrical and magnetic properties as well as aiding in the modification of their synthesis and development.

1.1.1. Nanoparticles

Nanoparticles in particular are of great interest since control over their size and solvents for dispersion can be achieved by the selection of coating. Popular methods for the development of monodisperse nanoparticles include the use of capping agents^[12] or surfactants^[13] that aid in stabilizing the nanoparticle suspension providing both protection of the core by the surface shell and creating a repulsive electrostatic or steric interaction between the formed nanoparticles to avoid aggregation. Functionalization of the surface chemistry can be manipulated to accommodate these desired parameters making them customizable. The following chapter focuses on ferrite spinel NPs coated with ricinoleic acid, a benign and inexpensive surfactant.

1.2. Magnetic Nanoparticles

1.2.1. Ferrites

Ferrites have attracted the interest of the scientific community due to their convenient synthesis and relatively large magnetic susceptibilities. Nanoparticle iron oxides are categorized as nanocrystals derived from magnetite ($\text{Fe(II)Fe(III)}_2\text{O}_4$) by introducing compatible metallic cations in the place of Fe(II), with significant magnetic saturation (M_s) up to $100 \text{ emu/g}^{[14]}$ at room temperature. At scales less than 20 nm in diameter they demonstrate superparamagnetic behavior in which the particles become magnetized in the presence of a magnetic field^[15]. The minute particles have sufficient thermal energy to overcome the anisotropic orientation of each particle acting as a magnet, leading to fluctuation of the magnetization resulting in a magnetic moment and zero net coercivity^[15].

1.2.3. Normal and Inverse Spinels

Spinels can be found abundantly in nature in gemstones and limestones in regions of Asia and Africa, in the form of Balas Ruby MgAl_2O_4 , for example. Additionally variations, such as, $(\text{Mg,Fe})(\text{Al,Cr})_2\text{O}_4$ are commonly found in peridotite, an igneous rock, in the uppermost earth's layer. These and other natural spinel examples have inspired the scientific community to pursue their synthetic development^[16].

A number of spinels are known today and can be prepared in a variety of compositions including magnetite $\text{Fe(II)Fe}_2\text{(III)O}_4$ (Fe_3O_4) an inverse spinel that contains Fe(III) on one-eighth of the tetrahedral sites (A) and one each of Fe(II) and Fe(III) on half of the octahedral sites (B) in a closely packed arrangement of oxide ions. Magnetite samples have measured magnetic susceptibilities between 92-100 emu/g^[17]. This configuration opens a path for a variety of spinels by clever introduction of divalent metals in one quarter of the “B” sites with a product having the same (inverse) spinel structure.

The first crystallographic characterization of a spinel is Bragg's magnesium aluminate MgAl_2O_4 spinel established in 1915^[18]. This structure demonstrated exceptional lattice stability, by achieving a cation to anion ratio of 3:4. In all spinels, the oxygen atoms have a face centered cubic structure with 32 octahedral and 64 tetrahedral interstitial sites in each unit cell (containing eight times the basic formula AB_2O_4). In a normal spinel the divalent cations “A” occupy tetrahedral sites, while the trivalent cations “B” occupy the octahedral sites^[8, 19], such that one-eighth of the tetrahedral sites and half of the octahedral sites are occupied. ZnFe_2O_4 , for example is a normal spinel and one of the structures to be discussed in this study.

On the other hand, Inverse spinels have a different cation distribution in which “B” sites are equally by divalent and trivalent cations, and the “A” sites have exclusively trivalent cations. Magnetite Fe_3O_4 and both CoFe_2O_4 and

NiFe_2O_4 , have this inverse spinel structure. Cobalt and Nickel ferrite, are ferromagnetic materials, whereas Zinc ferrite, demonstrates antiferromagnetic behavior due to their relative lattice interactions. Ferrites have ionic bonding, like all oxides, and their magnetic ordering tends to be antiferromagnetic, however differences exist depending on the cation arrangements in the magnetic lattice. The strongest magnetic interaction in this structure corresponds to “AOB” interactions in which A corresponds to the tetrahedral cations, B to the octahedral cation, and O to oxygen anions. Both Zn and Fe ions occupy octahedral sites with antiferromagnetically coupled Fe centers in the Zn ferrite resulting in a zero magnetization. In the case of the cobalt and nickel ferrite, the non-Fe cations occupy different sublattices resulting in an increase in the magnetization^[8, 19b].

Overall, in a spinel structure the addition of paramagnetic cations could lead to a higher magnetic susceptibility depending on the lattice interactions. The manipulation of cation occupations is a promising route for the optimization of ferrite spinel NPs to obtain maximum magnetic saturation..

1.3. Preparation Methods

Known preparation methods can be grouped into three different routes: chemical^[1b, 20], physical^[21], and biological^[22], in which the chemical route comprised approximately 90% of the publications. In this category, nanoparticle synthesis via precipitation comprises 27% of the chemical work in the literature, followed by hydrothermal and microemulsion methods^[20b]. These, and a few

other methods^[20a, 20e, 23], have been successful in the production of ferrite nanoparticles with narrow size distribution and stable dispersions both in aqueous and organic solvents.

1.3.1. Biological Methods

1.3.1.1. Biomolecule-Mediated Nanoparticles Self-Assembly

Nanoparticle self assembly can be achieved by the introduction of "molecular glues", biomolecules that bond at the nuclei surfaces forming in a precursor solution and aiding the formation of nanoparticles by bridging the nuclei at the interface and promoting growth of the nanoparticles. A recent example is the proteinaceous barnase–barstar interface method in which barnase-barstar bind to selectively functionalize particles^[22a]. This method has been shown to work for magnetic nanoparticle systems, however external stimuli such as pH variation will have an effect on the binding sites promoting disaggregation^[22a].

1.3.1.2. Biology Assisted Sol/Gel Process

Spinels can be synthesized by biology assisted sol/gel processes. In this method, stoichiometric portions of the precursors are introduced in a biological gel network, such as polysaccharide^[22b]. By combining gelling polymers and non-gelling ones synergistic effects rise, resulting in interactions among different polymer chains thus forming mixed junction zones ideal for nanoparticle

formation in the presence of desired precursors^[22b]. The product obtained from this reaction yields a precursor that would still need to undergo calcination.

1.3.2. Physical Methods

1.3.2.1. Ball Milling

In a ball milling process a mechanical device grinds solids into fine powders. Nanocrystalline ferrites have been successfully achieved via the ball milling process utilizing powder precursors and high temperature treatments (400 °C to 750 °C)^[21b]. Reported results show maximum magnetic saturation of ~70 emu/g^[21b], however size control has been difficult to achieve.

1.3.2.2. Mechanical Processes of Powder Mixture

The combination of mechanical processes have been demonstrated to be successful in the development of ferrite spinels as proven by the reported three stage process^[21d]. The first stage involves the reduction of the crystalline size and accumulation of defects, secondly, a nanoquasiamorphous state is formed, and lastly the final spinel phase is achieved. Nanoparticles are accomplished by solid-state temperature variation and annealing during the different stages. Results demonstrated formation of pure materials, however polydisperse and amorphous particles formed^[21d].

1.3.3. Chemical Methods

1.3.3.1. Co-Precipitation

Co-precipitation involves the simultaneous occurrence of nucleation and growth leading to coarsening processes. In general during co-precipitation processes insoluble species are formed under high supersaturation conditions, followed by nucleation in which a large number of small particles are formed leading to growth and secondary processes such as Ostwald ripening^[24] affecting drastically the size and morphologies of the products achieved. Particle nucleation is separated from particle growth by diffusion of the solute to the NP surface from the solution until the desired size is achieved. This process can be monitored via SEM (scanning electron microscopy) and manipulated by control over the starting cation concentration and pH variation in the solution as well as removal of mechanical forces acting in the mixture such as stirring. Metallic NPs can be formed from aqueous solutions by reduction from nonaqueous solutions. For example magnetite nanoparticles can be obtained from Fe(II)/Fe(III) precursors in the presence of a base^[25]. After overcoming the coarsening process, further reaction could result in the agglomeration of the formed particles causing larger non-uniform particles. NP size can be kept within 2-15 nm^[20c] in diameter, although aggregation and high polydispersity are likely to be observed.^[26]

1.3.3.2. Microemulsions

Two-phase methods are also broadly used for the preparation of ferrites^[1d]. Water/oil (W/O) microemulsions yield uniform, monodisperse nanoparticles by controlling the particle nucleation versus growth in solution. Nano-droplets of water are introduced and dispersed into an oil environment loaded with surfactants that arrange in the water/oil interphase to form cavities (~10 nm), thereby limiting the number of nucleation sites and avoiding aggregation. This process can achieve a wide range of nanoparticle sizes by altering the surfactant nature and concentration. Multiple surfactants can dictate the physical and chemical properties of the synthesized nanoparticles,^[1d, 20b, 26] however, the complexity of this method makes it difficult to scale up.

1.3.3.3. Sol-Gel

Sol-gel processes can also be utilized for the synthesis of ferrites such as in the development of iron oxide-silica aero gel composites.^[27] This result is achieved by hydroxylation and condensation of molecular precursors in solution yielding a dispersion of nanoparticles known as the “sol”. Subsequently, the solvent is removed to obtain a “gel” in which a three dimensional network of metal oxides is formed.^[27a, 28] While the synthesis is usually carried out in water; hydroxylation of the precursor can also be achieved with acid or base to produce different gel environments, polymeric for acid and colloidal for base ^[20b]. Nanoparticles synthesized by the sol-gel process form colloids and offer high

monodispersity as well as controlled particle dispersion and size distribution. However, contamination from the reaction's side products is often observed, e.g. residual polymer surfactant in the colloidal suspension, and post treatment or thermal decomposition of the nanomaterials is necessary for further polycondensation in order to obtain a crystalline state and enhance NP mechanical properties^[29].

1.3.3.4. Gas/Aerosol

Magnetic nanoparticles have been synthesized by spray pyrolysis by scattering a ferric salt and reducing agent scattering into a series of reactors. The solvent evaporates while the aerosol solute condenses, resulting in dried particles whose size is dependent on the concentration of the original solution, with sizes ranging from 5-60 nm having been reported^[21a, 30]. Monodisperse products with high magnetic susceptibilities can be achieved by precise control of the experimental conditions, however the instruments are expensive and contamination and gas phase, airborne particle impurities within the sample can also be observed^[27].

1.3.3.5. Polyol Method

The polyol method is more suitable for biomedical applications because of the ability to use biocompatible and biodegradable hydrogels during the process^[20a, 23, 31]. It is based on the control of the precipitation kinetics using

polyols, such as polyethylene glycol, as solvent. Polyols not only dissolve the inorganic precursor, but also function as stabilizing and reducing agents^[20a, 23]. This method demonstrates great control against aggregation and provides good particle growth during the synthesis. Furthermore, due to the high boiling points of polyols, the operating temperature can be manipulated in order to achieve dissolution of a number of inorganic precursors.

1.3.3.6. Thermal Decomposition

Crystalline iron oxide nanoparticles can be obtained by exposing organometallic precursors to high temperatures until their decomposition is achieved in the presence of stabilizers and in a medium with a high boiling point^[1e, 20d, 25, 32]. For example, iron oxide nanocrystals can be obtained by thermal decomposition of iron carboxylate salts utilizing oleic acid in a high temperature environment in order to generate iron carboxylate precursors^[20e].

1.3.3.7. Hydrothermal

Hydrothermal reactions are often carried out in aqueous media (even though organic solvents are also utilized) in autoclaves that can provide a high-pressure environment of up to 2000 psi and temperatures higher than 200°C under which conditions water can be hydrolyzed. The high temperature dehydrates the metal salt precursor, resulting in a metal oxide with low solubility in water. This environment is suitable for the supersaturation of the metal oxides and formation of nanoparticle dispersions^[1b, 1e, 26, 33]. *Parameter variation studies*

have been conducted to determine the effect that changing reagent concentration, reaction time, and temperature have on the nanoparticle size distribution and morphology. Changes in the concentration and temperature affect the physical properties of these materials, however a greater property dependence on the reaction time has been observed^[20b, 26].

Further studies described in this thesis demonstrate a pH dependence on the spinel nanoparticle size distribution and dispersities^[34]. Control over the particles' size and morphology, as well as the convenient one step, one pot synthesis procedure have been previously demonstrated to be ideal for the synthesis of ferrite spinels. The hydrothermal procedure carried out by the Doerrer group^[34] has been effective at lower temperatures than previously reported in the literature^[1b] and introduces an alternate surfactant to avoid nanoparticle aggregation and maintain stability^[34]. This thesis discusses the magnetic characterization of nanoparticles resulting from the Doerrer group's hydrothermal approach.

When choosing among the myriad synthetic processes available today for ferrite spinels such as: microemulsions^[10], hydrothermal^[1b], ball milling^[21b], sol/gel^[27a], to name a few, it is crucial to understand how the final product properties are affected by the choice of method. The nanoparticles' physical and chemical properties such as coating surface functionalization and chemical stability can be affected drastically by the parameters of the reaction process.

Once a synthetic route has been chosen, the precursor addition and concentration as well as surfactants and stabilizers, pH changes, temperature and time variations, all need to be optimized. It is also important to understand the limitation of the processes encountered in the literature, as described above, in order to find the best fit for our purposes. Narrow size distribution, uniform morphologies, synthesis scale-up ability, air stability, and production cost are the major properties of most interest for this research.

2.0. Experimental

2.0.1. General Procedures

All the reagents were obtained commercially and used as received, without further purification. The following characterization data has been collected by Fred Baddour^[34] for the samples indicated: (i) elemental composition data by means of an energy dispersive X-ray spectrometer (EDX) attached on a JEOL JSM-6100 scanning electron microscope (SEM), (ii) determination of particle size distribution by means of transmission electron microscope (TEM) recorded with a JEOL JEM-2010, and (iii) hydrodynamic radii by means of dynamic light scattering (DLS) measurements with a Brookhaven 90plus Nanoparticle Sizer.

2.1. Preparation Of Nanoparticles

The following procedures have been adapted from method previously developed by the Doerrer group^[34].

2.1.1. CoFe₂O₄•RA. Portions of Fe(NO₃)₃•9H₂O (0.641 mmol) and Co(NO₃)₂•6H₂O (0.320 mmol) were dissolved in DI water (3.00 mL). Concentrated (v/v= 65.0 mL/L) NH₄OH was added dropwise to the solution with vigorous stirring until a pH of ~ 9 was reached. The reaction mixture was stirred for 2 h and then transferred to a teflon-lined steel autoclave cell charged with toluene (3.0 mL) and ricinoleic acid (RA) (1.00 mL, 3.12 mmol). The autoclave was sealed and heated to 198 °C over 2 h. The temperature of 198 °C was then maintained for 10 h, after which the reaction mixture was allowed to cool to room temperature naturally. A dark brown dispersion of NPs in toluene was separated from a colorless aqueous layer by careful pipette extraction. The particles were precipitated from the organic layer of the reaction mixture *via* the addition of excess acetone. The resulting brown powder was magnetically separated with a hand-held neodymium magnet and the acetone was decanted. The particles were suspended and washed twice more with acetone before being redispersed in toluene for later use. The metal composition and hydrodynamic radii have been determined by Fred Baddour^[34]. The core was determined to be 7.1 ± 1.3 nm by EDX and their hydrodynamic radii in toluene was determined to be 15.6 ± 2.2 nm via DLS^[34].

2.1.2. NiFe₂O₄•RA. Portions of Fe(NO₃)₃•9H₂O (0.641 mmol) and Ni(NO₃)₂•6H₂O (0.320 mmol) were dissolved in DI water (3.00 mL). Concentrated (v/v= 65.0 mL/L) NH₄OH was added dropwise to the solution with vigorous stirring until a pH of approximately 9 was reached. The reaction mixture was stirred for 2 h and then transferred to a teflon-lined steel autoclave cell charged with toluene (3.0 mL) and ricinoleic acid (RA) (1.00 mL, 3.12 mmol). The autoclave was sealed and heated to 198 °C over 2 h. The temperature of 198 °C was then maintained for 10 h, after which the reaction mixture was allowed to cool to room temperature naturally. A brown dispersion of NPs in the toluene was separated from a colorless aqueous layer by careful pipette extraction. The particles were precipitated from the organic layer of the reaction mixture *via* the addition of excess acetone. The resulting brown powder was magnetically separated with a hand-held neodymium magnet and the acetone was decanted. The particles were suspended and washed twice more with acetone before being redispersed in toluene for later use. The metal composition and hydrodynamic radii have been determined by Fred Baddour^[34]. The core was determined to be 6.2 ± 1.2 nm by EDX and their hydrodynamic radii in toluene was determined to be 20.4 ± 2.5 nm via DLS^[34].

2.1.3. MnFe₂O₄•RA. Portions of Fe(NO₃)₃•9H₂O (0.641 mmol) and MnCl₂•4 H₂O (0.320 mmol) were dissolved in DI water (3.00 mL). Concentrated (v/v= 65.0 mL/L) NH₄OH was added dropwise to the solution with vigorous stirring until a pH of approximately 10 was reached. The reaction mixture was stirred for 2 h

and then transferred to a teflon-lined steel autoclave cell charged with toluene (3.0 mL) and ricinoleic acid (RA) (1.00 mL, 3.12 mmol). The autoclave was sealed and heated to 198 °C over 2 h. The temperature of 198 °C was then maintained for 10 h, after which the reaction mixture was allowed to cool to room temperature naturally. A brown dispersion of NPs in the toluene was separated from a colorless aqueous layer by careful pipette extraction. The particles were precipitated from the organic layer of the reaction mixture *via* the addition of excess acetone. The resulting brown powder was magnetically separated with a hand-held neodymium magnet and the acetone was decanted. The particles were suspended and washed multiple times with acetone before being redispersed in toluene for later use. The hydrodynamic radii in toluene was determined to be 41.39 ± 6.09 nm via DLS.

2.1.4. ZnFe₂O₄•RA. Portions of Fe(NO₃)₃•9H₂O (0.641 mmol) and ZnCl₂ (0.320 mmol) were dissolved in DI water (3.00 mL). Concentrated (v/v= 65.0 mL/L) NH₄OH was added dropwise to the solution with vigorous stirring until a pH of approximately 9 was reached. The reaction mixture was stirred for 2 h and then transferred to a Teflon-lined steel autoclave cell charged with toluene (3.0 mL) and ricinoleic acid (RA) (1.00 mL, 3.12 mmol). The autoclave was sealed and heated to 198 °C over 2 h. The temperature of 198 °C was then maintained for 12 h, after which the reaction mixture was allowed to cool to room temperature naturally. A dark brown dispersion of NPs in the toluene was separated from a colorless aqueous layer by careful pipette extraction. The

particles were precipitated from the organic layer of the reaction mixture *via* the addition of excess acetone. The resulting brown powder was magnetically separated with a hand-held neodymium magnet; left to settle then the acetone was decanted. This part of the procedure was repeated three more times due to weak magnetic response. The particles were suspended and washed multiple times with acetone before being redispersed in toluene for later use. The metal composition and hydrodynamic radii of the sample studied *via* VSM were not determined, however similar samples synthesized and characterized by Fred Baddour were determined to have a metal core of 6.7 ± 0.9 nm by EDX and hydrodynamic radii in toluene of 16.1 ± 2.0 nm via DLS^[34].

2.2. Preliminary Results

The Doerr group's resulting nanoparticles have precise compositions, narrow size dispersities, and thermal stability^[34]. Time and temperature dependent studies done by Fred baddour^[34] indicate that control over NP size is possible and, depending on the desired size, syntheses in only 2 h are needed^[34]. Currently, the hydrothermal synthesis yields about 100 mg per batch, but scale up by a factor of ten should be feasible.

Initial syntheses demonstrated good magnetic response from the Co and Ni nanoparticles as well as high monodispersity as shown in Figure 1.1. for a CoFe_2O_4 -RA sample, and were optimized by a series of time and pH variations^[34]. The metallic composition was found to be 1:2 $\text{M}^{\text{II}}:\text{Fe}$, as determined

via EDX spectroscopy^[34]. The particle core diameters were determined with TEM, and the hydrodynamic radii determined via DLS. The TEM micrographs demonstrated the morphology of the MFe_2O_4 particles, with core size distributions averaging 6.2 to 7.5 nm and hydrodynamic radii between 8.9-19nm^[34]. Further optimization of the $MnFe_2O_4$ and $ZnFe_2O_4$ NPs syntheses was required at this stage before moving forward with the VSM studies. Initial results demonstrated poor magnetic response and dispersion as well as low stability over time as shown in Figure 1.2. for a $ZnFe_2O_4$ -RA sample.



Figure 1.1. Dispersity and magnetic response of $CoFe_2O_4$ -RA sample after 6 months



Figure 1.2. Low dispersity and magnetic response of $\text{ZnFe}_2\text{O}_4\text{-RA}$ in toluene after 3 months

2.3. Synthesis Optimization- $\text{MnFe}_2\text{O}_4\text{-RA}$ and $\text{ZnFe}_2\text{O}_4\text{-RA}$ NPs

Additional studies were conducted varying the pH used to prepare the sol-gel mixture and reaction time (shown in Table 1.1. and Table 1.2. respectively) to optimize the dispersion and magnetic susceptibility of the $\text{MnFe}_2\text{O}_4\text{-RA}$ and $\text{ZnFe}_2\text{O}_4\text{-RA}$ NPs.

Table 1.1. pH Dependence Analysis of MnFe₂O₄-RA and ZnFe₂O₄-RA**Syntheses**

Compound	Temp (°C)	Duration (h)	pH	Observations
MnFe₂O₄-RA	198	10	9	Poor quality, low magnetic response, solubility and stability over time
	198	10	10	Best Batch, good magnetic response and solubility
	198	16	9	Poor quality, low magnetic response, solubility and stability over time
	198	16	10	Poor quality, low magnetic response, solubility and stability over time
ZnFe₂O₄-RA	198	10	9	Poor quality, low magnetic response, solubility and stability over time
	198	10	10	Poor quality, low magnetic response, solubility and stability over time
	198	12	8	Need modification, some magnetic response, poor dispersion
	198	12	10	Need modification, some magnetic response, poor dispersion

Table 1.2. Time Dependence Analysis of MnFe₂O₄-RA and ZnFe₂O₄-RA syntheses

Compound	Temp (°C)	Duration (h)	pH	Observations
MnFe₂O₄-RA	198	5	10	Poor quality, low magnetic response, solubility and stability over time
	198	10	10	Best Batch, good magnetic response and solubility
	198	12	10	Need modification, some magnetic response, some solubility issues
	198	16	10	Poor quality, low magnetic response, solubility and stability over time
ZnFe₂O₄-RA	198	5	10	Poor quality, low magnetic response, solubility and stability over time
	198	10	10	Poor quality, low magnetic response, solubility and stability over time
	198	12	10	Need modification, some magnetic response, poor dispersion
	198	16	10	Poor quality, low magnetic response, solubility and stability over time

Based on observations above, MnFe₂O₄-RA samples synthesized at pH 10 and maintained temperature of 198 °C for 10 h, resulted in magnetically responsive, stable dispersions in toluene fit for magnetic susceptibility studies.

The ZnFe₂O₄-RA synthesis, however proved more challenging. The best results were obtained at pH 8 and pH 10 when maintained at a temperature of 198 °C for 12 h from which some magnetic response was observed with low dispersity in toluene. Magnetic susceptibility studies were conducted for ZnFe₂O₄-RA samples synthesized at approximately pH 8, pH 9 and pH 10 for a close comparison of the magnetic susceptibility of this species.

2.4. Nanoparticle Characterization

The TGA curves of the samples were obtained from a Perkin Elmer TGA (Thermogravimetric analyser) located in the Ceramic Processing Research Laboratory (CPRL) at MIT. The 50 µL samples were placed in a Pt pan and measured at a heating rate of 10 °C/min.

2.4.1. Sample Preparation for TGA:

Toluene was utilized as solvent for the dispersion of the samples, while keeping accurate records of the volumes and concentration for further use. A 100 µL aliquot of the sample was pipetted onto a platinum-weighting pan making sure the mixture was well dispersed.

2.4.2. TGA General Procedures:

The instrument balance was tared by weighing the empty pan prior to taking any measurements. Subsequently the pan was loaded with the sample aided by a load tray cell. Making sure to position the load tray cell directly below the pan, the tray was raised slowly until the tray supported the weight of the pan. Once the sample pan was securely in place, a mobile furnace was raised covering the pan and stem completely. To avoid inconsistency in the measurements the furnace chamber was purged with nitrogen gas. The temperature program was then set to the desired rate (10 °C/min) and maximum temperature of 800 °C. Once the settings were satisfactory, a thermogram was generated indicating the weight lost as demonstrated in Figure 3.

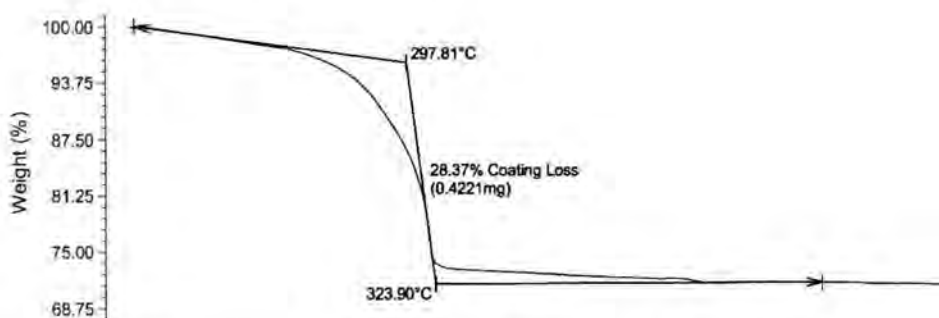


Figure 1.3. TGA thermogram of $\text{CoFe}_2\text{O}_4\text{-RA}$ in % mass versus temperature

2.4.3. Sample Calculations:

The thermogram indicates the solvent and coating masses lost and the stabilized final mass. The mass lost is calculated by subtracting the final from the initial.

TGA data in terms of mass (%):

$$\text{Mass \%} = \text{Initial} - \text{Final}$$

$$\% = 100 - 71.63 = 28.47 \% \text{ (as shown in **Figure 1**)}$$

TGA data in terms of Weight (mg):

$$\text{Weight \%} = \text{Initial (mg)} - \text{Final (mg)} \times 100$$

Obtaining sample weight:

The TGA data provides the unsubtracted weight of the sample measured for the completed run.

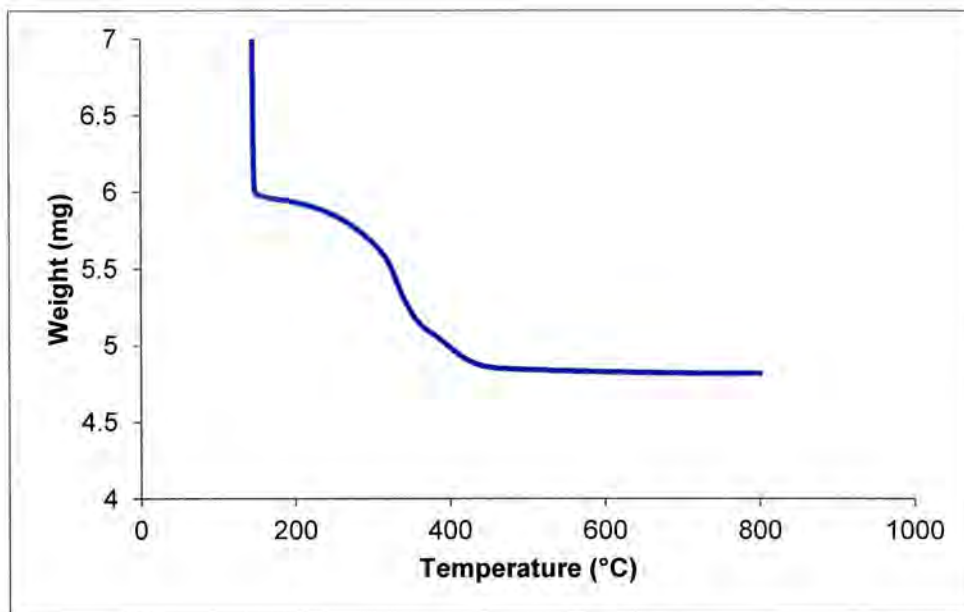


Figure 1.4. TGA thermogram of $\text{CoFe}_2\text{O}_4\text{-RA}$ in terms of absolute mass (mg) vs. Temp. ($^{\circ}\text{C}$)

For the sample in Figures 1.3. and 1.4. the weight of the CoFe_2O_4 core was 4.82 mg in 100 μL of solution.

2.4.4. Vibrating Sample Magnetometer

The Vibrating Sample Magnetometer (VSM) data were collected on a Lakeshore vibrating sample magnetometer located at the Dana Research Center, in Professor Nian Sun's group at Northeastern University. Measurements were carried out at room temperature at 2.0 seconds per data point with 200

points per sample. A 10 μL portion of the sample was drop-cast onto a 0.5 cm^2 glass or silica substrate and solvent left to evaporate at room temperature. This process was repeated until a uniform thin film of the sample was obtained. The sample was then mounted onto the sample tube and subsequently inserted into the sample chamber suspended between two electromagnets. The sample was exposed to a uniform magnetic field and was then vibrated sinusoidally. All materials studied exhibited a hysteresis curve in the plot of magnetization (emu=electromagnetic unit) (Y axis) versus increasing magnetic field (G=Gauss) (X axis).

2.4.5. Vibrating Sample Magnetometer (VSM) Calculations:

Calculations for converting electromagnetic unit (emu) to emu/g using the mass obtained from the TGA thermogram for a CoFe_2O_4 -RA sample.

Fixing mass/volume ratio:

For the VSM the volume utilized for the run was 10 μL of solution, in order to find the weight of CoFe_2O_4 in 10 μL , a ratio comparison is established:

$$100 \mu\text{L} = 4.82 \text{ mg}$$

$$10 \mu\text{L} = X$$

$$X = \frac{10\mu\text{L} \times 4.82\text{mg}}{100\mu\text{L}} = 0.482\text{mg}$$

Now the value in milligrams (mg) can be converted into grams (g):

$$1\text{g} = 1000\text{mg}$$

$$X = 0.482\text{mg}$$

$$X = \frac{1\text{g} \times 0.482\text{mg}}{1000\text{mg}} = 0.000482\text{g}$$

Finally this value can be used to convert the electromagnetic units (emu) into (emu/g):

$$\frac{0.002446\text{emu}}{0.000482\text{g}} = 5.08\text{emu/g}$$

The results are then plotted to obtain the VSM graph as demonstrated in Figure 1.5. below.

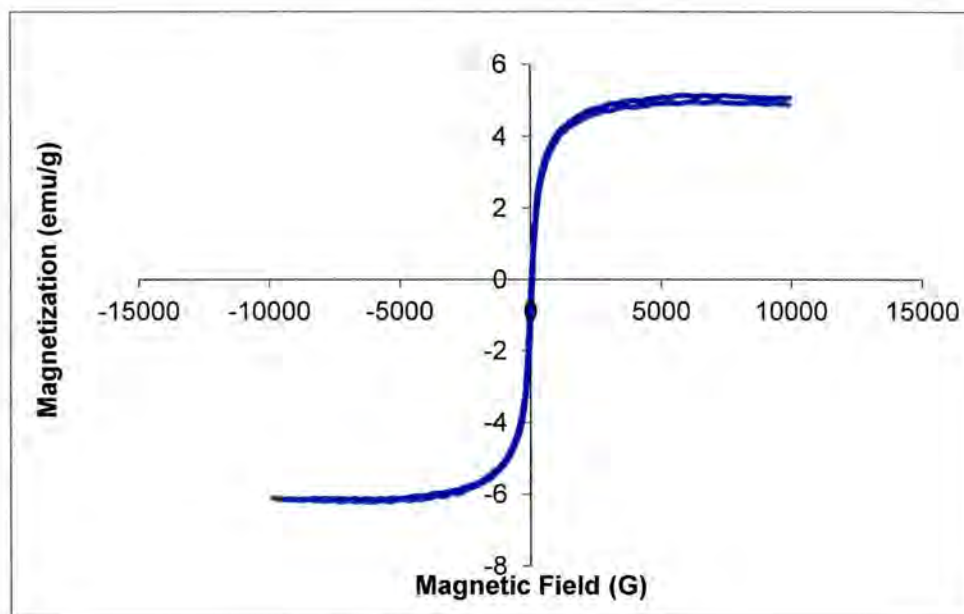


Figure 1.5. VSM hysteresis curve of $\text{CoFe}_2\text{O}_4\text{-RA}$

3.0. Results and Discussion

The magnetic saturation values of $\text{CoFe}_2\text{O}_4\text{-RA}$, $\text{NiFe}_2\text{O}_4\text{-RA}$, $\text{MnFe}_2\text{O}_4\text{-RA}$ and $\text{ZnFe}_2\text{O}_4\text{-RA}$ have been quantitatively determined via VSM studies up to a maximum magnetic field of 1000 G and their NP metal core composition was determined via TGA.

3.1. TG Analysis of $\text{CoFe}_2\text{O}_4\text{-RA}$, $\text{NiFe}_2\text{O}_4\text{-RA}$ and $\text{MnFe}_2\text{O}_4\text{-RA}$

3.1.1. Cobalt Ferrite, $\text{CoFe}_2\text{O}_4\text{-RA}$ Figure 1.4. shows the TGA curve for $\text{CoFe}_2\text{O}_4\text{-RA}$ dispersed in toluene. The decomposition consists of three distinct

regions of 100-150°C, 150- 425°C and 425-783°C. The first weight loss region from 100-150°C is indicative of the loss of toluene (b.p. = 110°C). The second weight loss region of 150- 425°C is attributed to the loss of the carboxylate coating resulting from the ricinoleic acid (b.p. = 416°C). In the third region at 425-600°C only the spinel phase remains (4.85 mg). Furthermore, after 600°C no further weight loss is seen up to 800°C

3.1.2. Nickel Ferrite, $NiFe_2O_4$ -RA Figure 1.6. shows the TGA curve for $NiFe_2O_4$ -RA dispersed in toluene. The decomposition followed the same general form as the Co-spinel and yielded 5.68mg, though temperatures above 550°C were not tested.

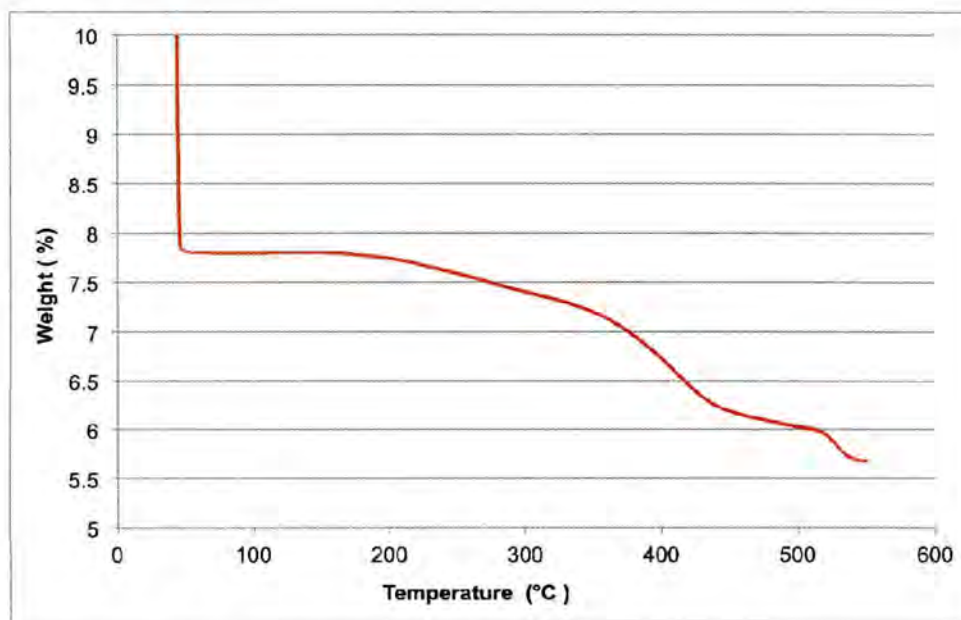


Figure 1.6. TGA thermogram of $NiFe_2O_4$ -RA

3.1.3. Manganese Ferrite, $MnFe_2O_4$ -RA Figure 1.7. shows the TGA curve for $MnFe_2O_4$ -RA dispersed in toluene. The decomposition followed the same general form as the Co-spinel and yielded 0.66 mg.

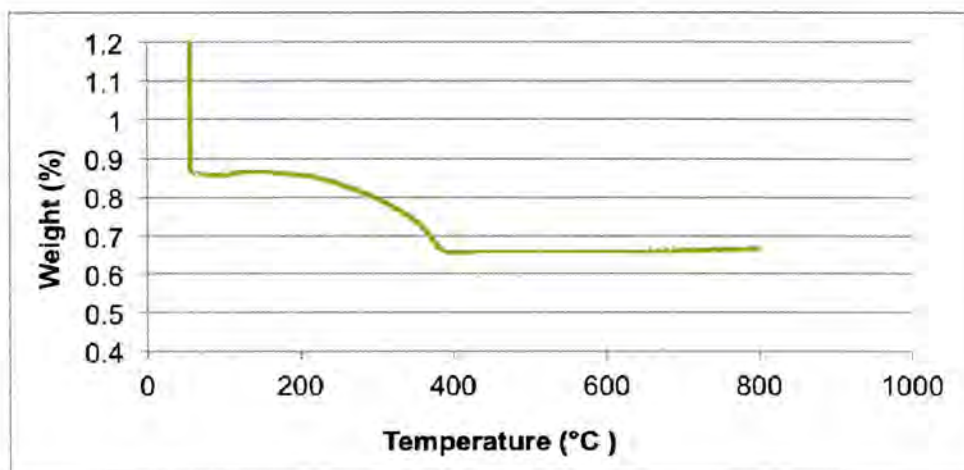


Figure 1.7.. TGA thermogram of $MnFe_2O_4$ -RA

3.2. VSM Analysis of $CoFe_2O_4$ -RA, $NiFe_2O_4$ -RA and $MnFe_2O_4$ -RA

3.2.1. Cobalt Ferrite, $CoFe_2O_4$ -RA Figure 1.5. plots the magnetization versus field for a sample with hydrodynamic radii of 22.4 ± 0.34 nm and metallic concentration of 4.85 mg. The magnetic saturation has been determined to be 5.06 emu/g based on the calculation method described above (Table 3). The NPs demonstrated affinity for a Nd magnet during the sample preparation, however the low magnetic saturation obtained suggests the presence of a cobalt

oxide phase, which is antiferromagnetic at room temperature^[3], this phase can be a product of sample preparation during desolvation of the NPs and can be identify by XRD (X-ray diffraction)^[35]. In addition, previous cobalt ferrites studies have demonstrated a correlation between the nanoparticles size and magnetic saturation^[2a] since larger metallic cores result in higher magnetic susceptibility, indicating that the small size of the nanoparticles studied could have an affect on the results.

3.2.2. Nickel Ferrite, $NiFe_2O_4$ -RA Figure 1.8. is analogous to Figure 1.5. The magnetic saturation (M_s , Table 3) has been determined to be 55.9 emu/g with hydrodynamic radii of 25.0 ± 0.23 nm and metal mass of 5.68 mg The NPs exhibit a magnetic saturation similar to that of its bulk counterpart ~ 50 emu/g^[36] and other NP data^[1a]. The difference in magnetic susceptibly compared to that of magnetite can be attributed to the substitution of d^8 Ni(II) in the octahedral sites for Fe(II).

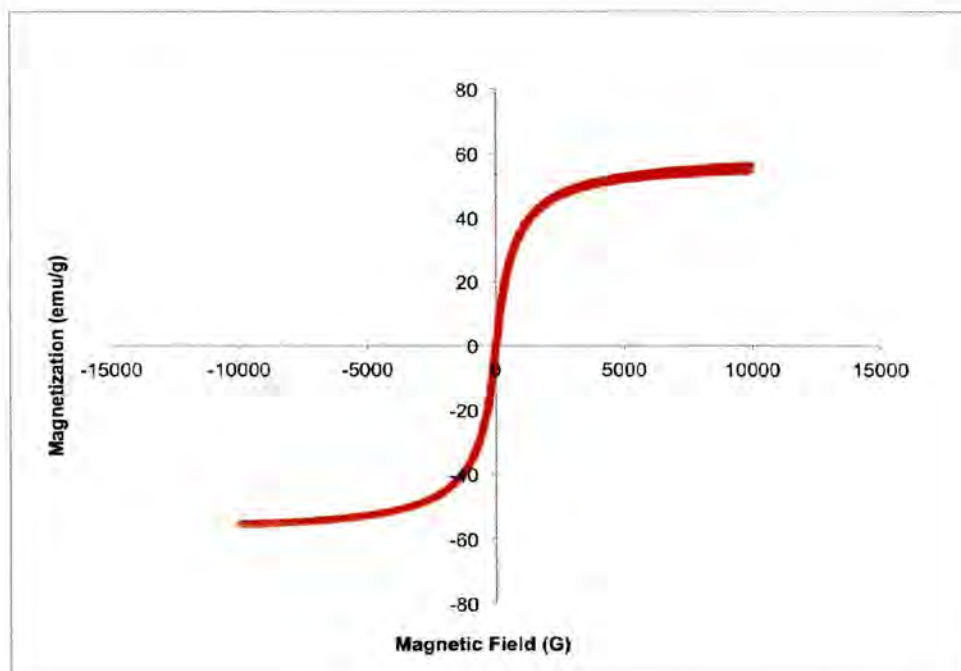


Figure 1.8. VSM hysteresis curve of $\text{NiFe}_2\text{O}_4\text{-RA}$

3.2.3. Manganese Ferrite, $\text{MnFe}_2\text{O}_4\text{-RA}$ Figure 1.9. is analogous to Figure 1.5. The magnetic saturation (M_S Table 3) has been determined to be 48.8 emu/g for a sample with hydrodynamic radii of 41.39 ± 6.09 nm and metal mass of 0.66 mg. The NPs exhibit a magnetic saturation comparable to literature examples ranging between 20-50 emu/g^[1c-e].

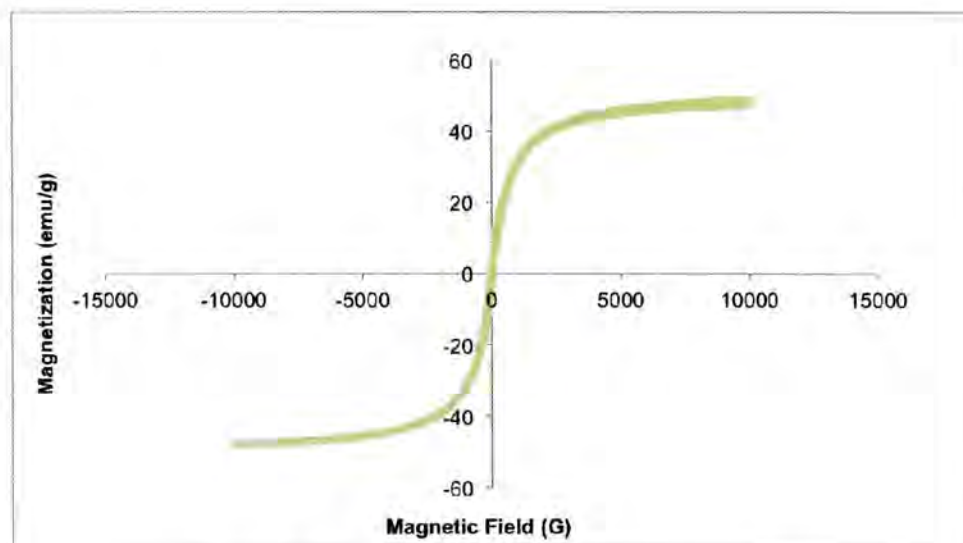


Figure 1.9. VSM hysteresis curve of MnFe₂O₄-RA

3.2.4. Comparison of CoFe₂O₄-RA, NiFe₂O₄-RA and MnFe₂O₄-RA M_S

As shown in Figure 1.10, a substantial difference in the magnetic saturation values of the NP cores was observed for three different samples. The magnetic properties of the Ni and Mn ferrites have demonstrated similar magnetic behavior to that of NPs developed with the capping agent oleic acid for the same spinel species (Table 1.3.). This similarity has not been the case for the Co samples for reasons not yet understood.

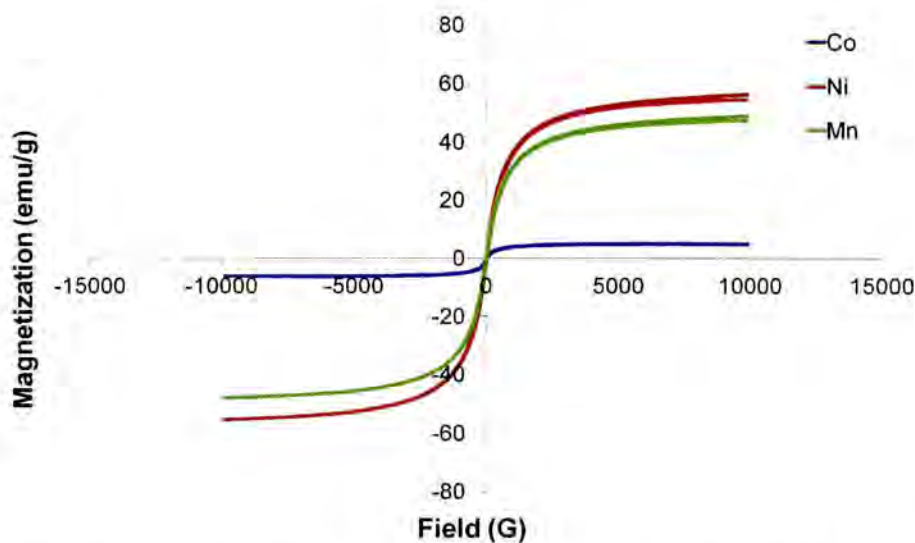


Figure 1.10. Comparative VSM hysteresis curves for $\text{CoFe}_2\text{O}_4\text{-RA}$ (Blue), $\text{NiFe}_2\text{O}_4\text{-RA}$ (Red) and $\text{MnFe}_2\text{O}_4\text{-RA}$ (Green)

Table 1.3. VSM and DLS data

$\text{MFe}_2\text{O}_4\text{-RA}$	M_s (emu/g)	Size by DLS (nm)	M_s Literature (emu/g)
$\text{CoFe}_2\text{O}_4\text{-RA}$	5.03	22.4 ± 0.34	$\sim 6\text{-}90^{[1b, 2]}$
$\text{NiFe}_2\text{O}_4\text{-RA}$	55.9	25.0 ± 0.23	$\sim 50\text{-}60^{[36][1a][1b]}$
$\text{MnFe}_2\text{O}_4\text{-RA}$	48.8	41.39 ± 6.09	$\sim 20\text{-}50^{[1b-e]}$

3.3. TG Analysis of $\text{ZnFe}_2\text{O}_4\text{-RA}$

3.3.1. Zinc Ferrite, $\text{ZnFe}_2\text{O}_4\text{-RA}$ Figure 1.11. shows the TGA curve for $\text{ZnFe}_2\text{O}_4\text{-RA}$ dispersed in toluene. The decomposition followed the same general form as the Co-spinel and yielded 0.37 mg.

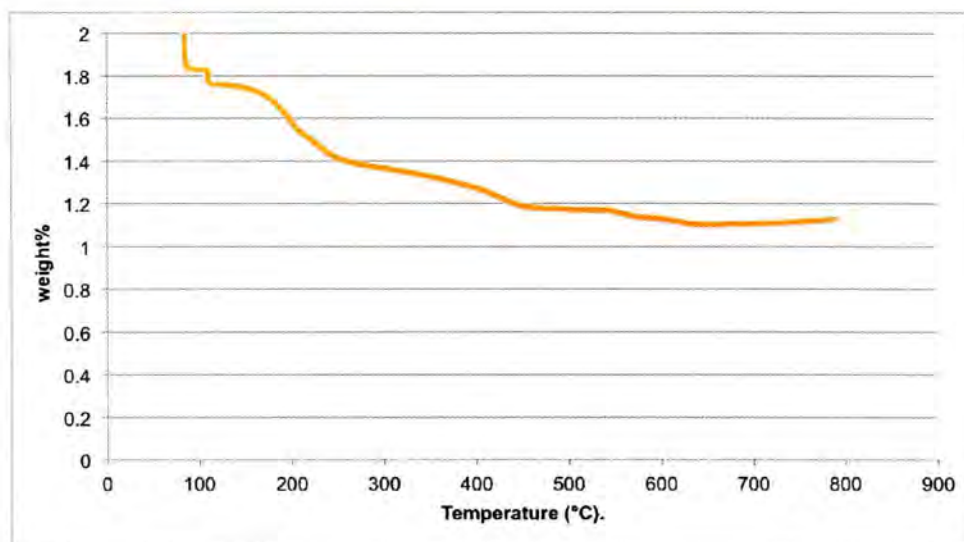


Figure 1.11. TGA thermogram of ZnFe₂O₄-RA

3.4. VSM Analysis of ZnFe₂O₄-RA at Different pH Values

3.4.1. Zinc Ferrite, ZnFe₂O₄-RA Figure 1.12. is analogous to Figure 1.5.

The magnetic saturation (M_S) has been determined to be 4.3 emu/g for a sample developed at ~ pH 9 and metal core mass of 0.37 mg.

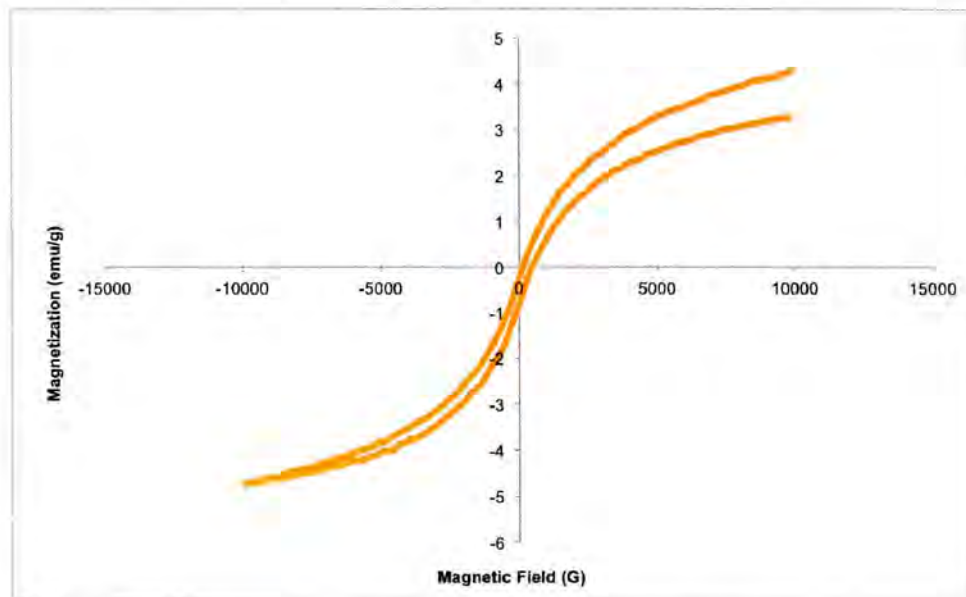


Figure 1.12. VSM hysteresis curve of $ZnFe_2O_4$ -RA with synthesis conditions: pH ~ 9, 10 h

3.4.2. Zinc Ferrite, $ZnFe_2O_4$ -RA Figure 1.13 is analogous to Figure 1.5..

The magnetic saturations (M_s) were determined to be 13.48 and 17.7 emu/g for samples developed at ~ pH 10 and pH 8 respectively and metal core mass of 0.37 mg.

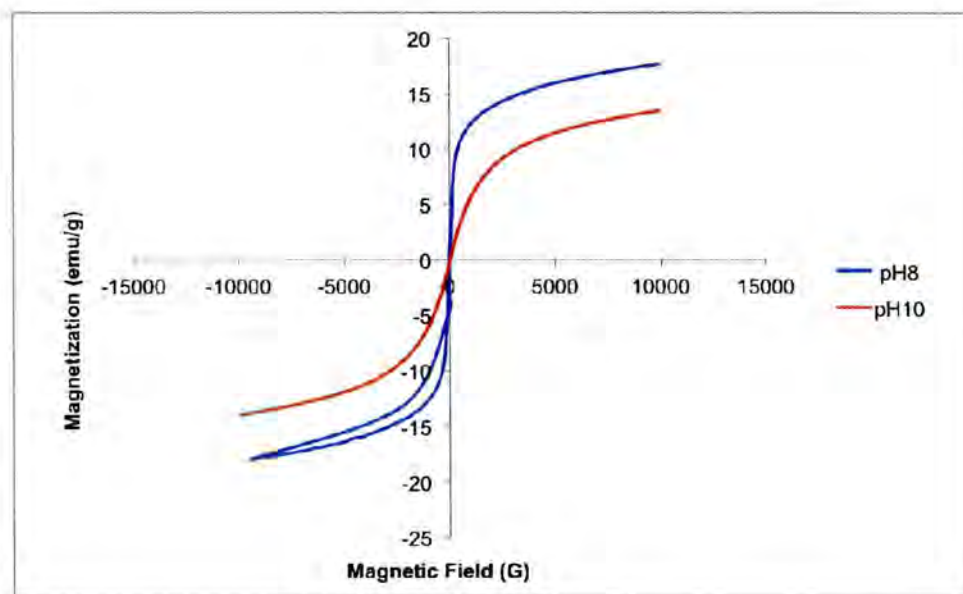


Figure 1.13. VSM hysteresis curve of $\text{ZnFe}_2\text{O}_4\text{-RA}$ at pH8 (Blue) and pH10 (Red)

3.4.3. Comparison of $\text{ZnFe}_2\text{O}_4\text{-RA}$ M_s as a Result of pH Variation

Figure 1.12 shows the magnetic properties of $\text{ZnFe}_2\text{O}_4\text{-RA}$ for the synthesis carried out at a pH of 9 and during a reaction time of 10 h. Further studies varying these synthesis conditions were also investigated by VSM as demonstrated in Figure 1.13. The nanoparticle suspension was determined to have better stability at longer reaction duration as well as higher magnetic susceptibility. Variation of pH also had an effect on the magnetic saturation as seen in Figure 1.13. At pH \sim 8, the $\text{ZnFe}_2\text{O}_4\text{-RA}$ sample had a higher magnetic saturation than at pH \sim 10 (17.7 and 13.48 emu/g respectively), however the

sample prepared at pH ~ 9 anomalously demonstrated the lowest M_S (4.3 emu/g).

4.0. Conclusions

The vibrating magnetic susceptibilities of a series of ricinoleic acid coated non-magnetite spinels with the form MFe_2O_4 ($M = Co, Ni, Mn, Zn$) have been studied. Two main results have been discussed: (1) Results indicate similarities between the magnetic saturation susceptibility (M_S) values obtained for Ni and Mn samples (55.9 emu/g and 48.8 emu/g, respectively), and published values for oleic acid, and other surfactant, coated species (~50 emu/g and ~20-50 emu/g respectively). Co samples demonstrated a low M_S of 5.06 emu/g in comparison to published results (~6-90 emu/g^[1b, 2]) that can be attributed to small core size and/or presence of other species, such as cobalt oxide, during measurements. (2) The Zn samples demonstrated dispersion difficulties and low magnetic susceptibility leading to a series of pH dependent studies resulting in a maximum M_S of 17.7 emu/g at pH ~ 8.

As stated previously in this chapter, in sections 1.3 and 2.2, variation of temperature, reaction duration, pH, surfactant concentration, precursor ratios, can influence the final size, stability and magnetic properties of the nanoparticles synthesized. The study discussed explored pH range variation and duration of reaction followed by magnetic susceptibility characterization. However further

studies could include magnetic susceptibilities of samples prepared with a wider range of pH, reaction duration, precursors ratio and temperature variation to get an in depth understanding of how these conditions, along with close size monitoring, affect magnetic properties of the ferrite spinels.

Chapter II. Microfabrication of a Four Point Device for Nanowire Electronic Conductivity Measurement

1.0. Introduction-Motivation

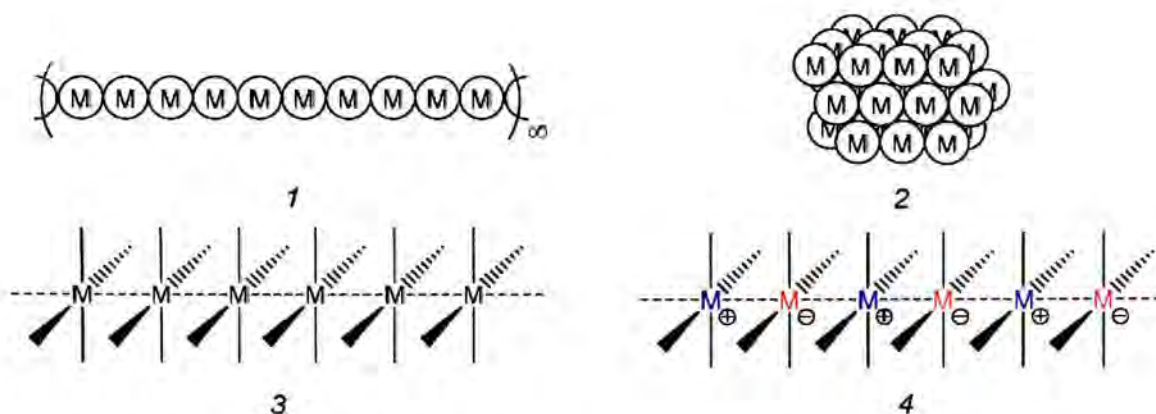
The development of one-dimensional (1D) nanowires has attracted interest due to their possible integration into various electronic devices. The Doerrer group is investigating the preparation of electrically conductive, one-dimensional, one atom wide nanowires employing a bottom-up approach. The goal is to use small molecule synthesis to attain an infinite chain of metal atoms protected by carefully chosen ligands. In this vision, electron transfer occurs through the atomic chain and the stabilizing ligands are an insulating layer. This ambitious concept has not yet been achieved; however, its accomplishment could provide an alternative approach to complementary metal-oxide-semiconductor (CMOS) microelectronic technology.

The inspiration for this research comes from the constantly decreasing size of electronic devices. Moore's Law describes this phenomenon as a linear relationship between decreasing transistor size (and the number of transistors per chip) and development time.^[37] Our society is saturated with electronic devices containing silicon-based chips with a minimum size ultimately limited by the size of silicon atoms. A closer look into any modern device would reveal that the wire is the most common and basic component utilized for every function. Electronic devices depend on efficient current flow, making it all the more important to develop improved wires.

Early examples of linearly arrayed structures with metal-metal contacts can be traced back to Magnus' Green Salt (MGS) in the 19th century. MGS, or

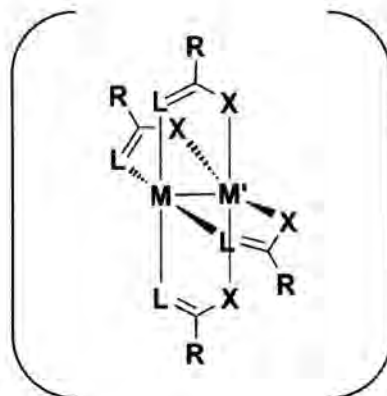
tetraammineplatinum(II) tetrachloroplatinate(II) $[\text{Pt}(\text{NH}_3)_4][\text{PtCl}_4]$ is composed of alternating cations and anions that contain Pt(II).^[38] Although this structure demonstrates the potential arrangement of the chain of atoms, it is an extremely insoluble semiconductor, making it difficult to process with solution-based techniques.^[39] Other researchers have explored linearly arrayed compounds, such as the Ritter group's synthesis of one-dimensional palladium wires at Harvard University.^[40] However, the development of a 1D nanomaterial that is stable under ambient conditions, as well as having excellent electronic conduction properties, has yet to be realized.

In order to control the formation of these infinite structures, one must prevent aggregation. A group of metal atoms in a linear array would not be stable thermodynamically relative to a cluster as illustrated in structure 2 in Scheme 2.1. However, the incorporation of moieties bonded orthogonally to the metal centers, 3, could prevent aggregation and provide stability as well as the incorporation of alternating metal ligands with opposite charges by electrostatic forces as seen in structure 4 Scheme 2.1. These interactions with ligands stabilize each metal center and facilitate assembly of aligned structures.



Scheme 2.1. 1) Linear array of atoms 2) Cluster of atoms 3) Stabilized structure with orthogonal bonding to ligands 4) Stabilization by electrostatics^[41]

With this understanding, a family of lantern structures has been developed by selecting a ligand system with two different donor atoms, one soft L donor (S) and one hard X donor (O), which favors distinct metal binding by exploiting the difference in binding affinities of M:Pt and M':3d metals for hard and soft bases. The success of this approach lies in the coordination environment control by selecting a four coordinate, square-planar ligand system that also favors metal-metal interactions. Considering the proposed parameters, thiocarboxylate ligands were ideal for the development of our desired structure.^[42] A lantern structure with two different divalent ions was attained with the following coordination environments: $[MS_4]$ and $[M'O_4]$ (as seen in Scheme 2.2.).



Scheme 2.2. Illustration of lantern unit demonstrating the L (S), X (O) donors and their binding affinity^[41]

These heterobimetallic lanterns are obtained via one-pot syntheses in water and can be recrystallized from organic solvents. The Doerrer group has prepared a series of lanterns of the form $[\text{PtM}(\text{tba})_4(\text{OH}_2)]$ ($\text{M}' = \text{Fe}^{[43]}$, $\text{Co}^{[43]}$, $\text{Ni}^{[43]}$, $\text{Zn}^{[34]}$) (tba= thiobenzoate). X-ray diffraction studies of the cobalt and nickel compounds revealed a $\text{Pt}\cdots\text{Pt}$ distance of 3.0650(3) Å and 2.570(1) Å respectively^[43], demonstrating the formation of short $\text{MPt}\cdots\text{PtM}$ sequence by dimeric metallophilic interactions.^[44]

The execution of the Doerrer group's hard/soft approach with thiocarboxylates to prepare heterobimetallic compounds has opened the path to the next synthetic stages of this project. Moving forward, it is crucial to extend the chains of lanterns while fomenting electrical conductivity. In order to accomplish this design, a π -acceptor bridging ligand has been introduced. For example, pyrazine has been shown to bridge metal centers such as $\text{Pd}^{[45]}$ and

Rh^[46], without disturbing the lantern structures.^[46] Unpublished work^[47] has already resulted in the structurally characterized compounds bridged by pyrazine [PtM(tba)₄(NC₄H₄N)]_∞ (M= Co, Ni, and Zn). These structures consist of an infinite array of lantern complexes linked by pyrazine units as shown in Figure 2.1. This series of bridged structures has been chosen for the study of their electronic conductivity in the solid state as well the study of the Zn derivative as control due to diamagnetic nature of Zn.

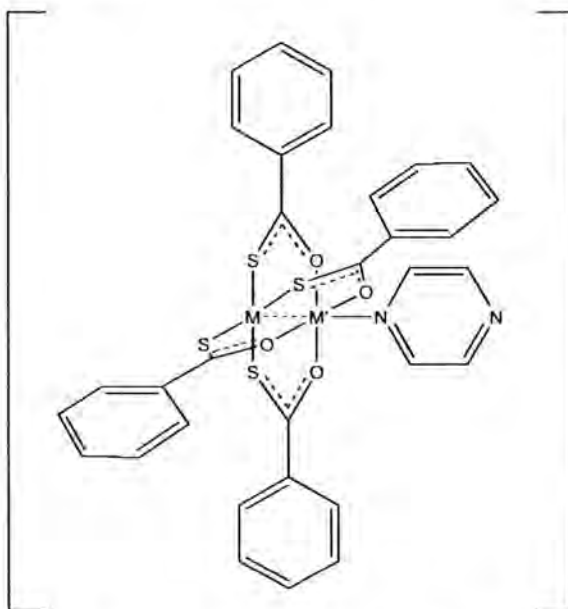


Figure 2.1. Structure of [MM'(tba)₄(pyZ)]

This chapter describes the design and development of a substrate for four-point probe electronic conductivity measurements with sub-micrometer scale Au wires utilizing microfabrication techniques for the characterization of the aforementioned pyrazine-bridged structures. The design shown in Figure 2.2

allows the user to deposit a sample on the micrometer scale Au contacts without the need for submicron probes, and is proposed to facilitate data collection while working with structures of diminutive dimensions. The bottom features in Figure 2.2. illustrates the Au wire dimensions, carefully designed to align with the instrument tips providing a constant separation (S) required for accurate resistivity calculations.

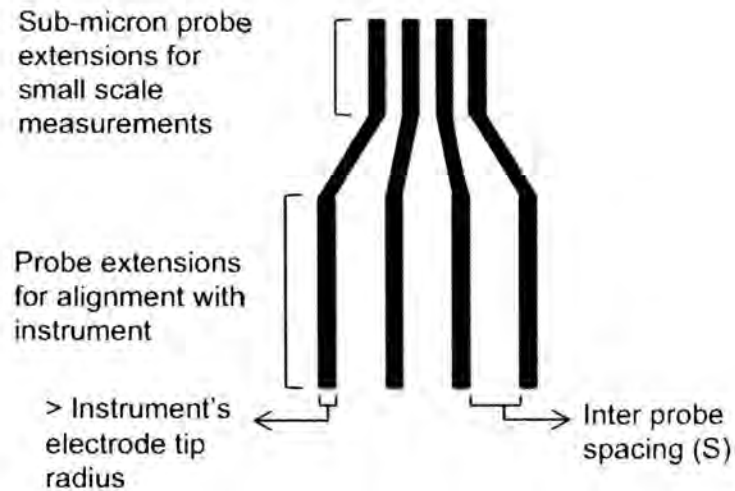
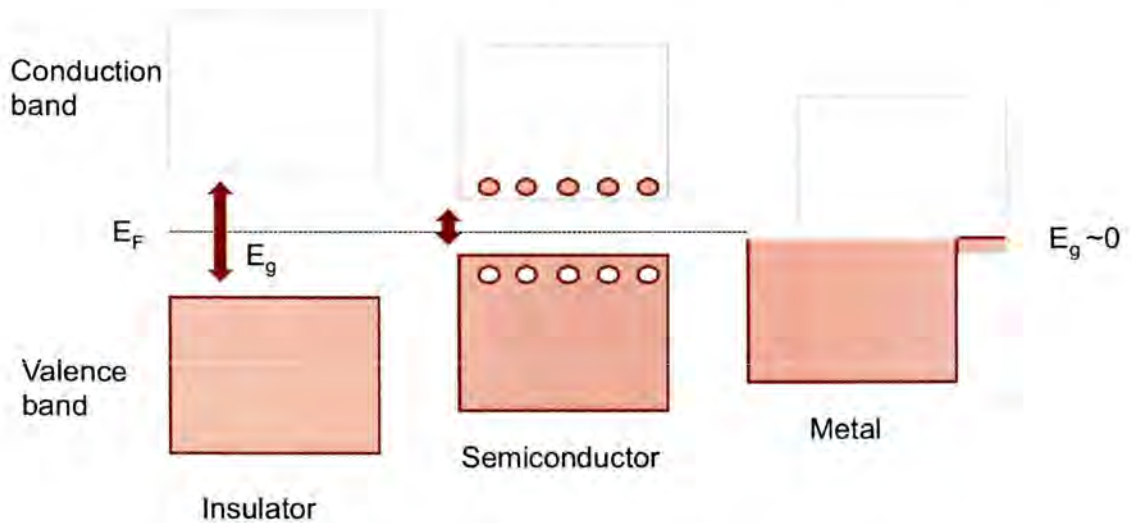


Figure 2.2. Proposed design for micro-fabricated Au electrodes for four-point measurement

2.0. Band Theory

Band theory allows us to understand what degree of electrical conductivity can be achieved according to the energy differences between the valence and conduction bands in the solid of interest. Scheme 2.3. illustrates the band

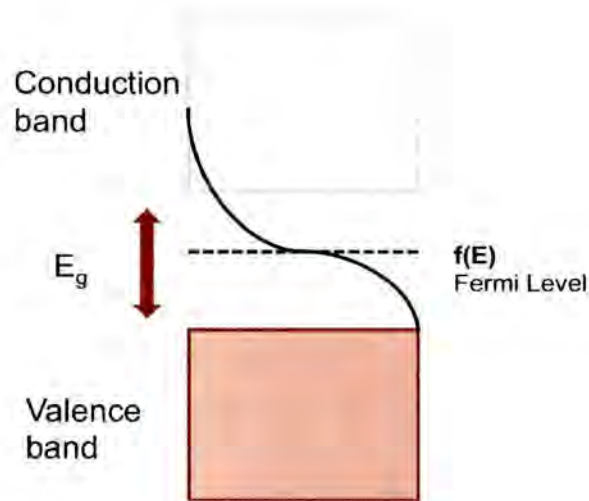
structure of three classes of solids: insulators, metals and semiconductors. In an insulator, a substantial energy gap is present between the occupied valence band and the unoccupied conduction band. For conducting materials, such as metals, overlapping valence and conduction bands are present, and permit facile electron transport. A semiconductor can act either as an insulator or a conductor depending on the temperature of the solid. An energy gap exists between the valence and conduction bands, however it is small enough that it can be overcome by thermal excitation of the electrons. The conductivity can be further manipulated by chemical doping in the lattice to reduce the effective band gap.



Scheme 2.3. Illustrations of band gaps for different materials

To determine the electronic properties of a material, it is important to understand the relationship of the Fermi level to the conduction band. The Fermi level can be described as the energy of the highest occupied electron level in the

solid at absolute zero^[48]. In metals, the Fermi energy provides information regarding the velocities of the electrons participating in conduction since only electrons close to the Fermi energy can contribute^[48].



Scheme 2.4. Illustration of the Fermi level for the electrical conductivity of a semiconductor as a function of temperature

If we consider a semiconductor solid, the idea of a band gap between the Fermi level and the conduction band is simple to picture. With increasing temperature, the number of electrons able to bridge the energy gap increases (as illustrated in Scheme 2.4) resulting in an increased electrical conductivity. The electron population in this case depends on the Fermi function (the probability that a particular electron energy state will be occupied at a specific temperature),

and the density of electronic states (the number of electron states per unit energy). At room temperature the density of states and the Fermi function have finite values in the conduction band, resulting in a finite conducting electron population^[48].

With the successful development of a four-point probe device, specifically designed to accommodate submillimeter samples, characterizing the Doerrer group one-dimensional nanowires is feasible. Measuring the conductance values will allow us to calculate the band gap for these compounds. Understanding the relationship of the band gap in a particular material and its temperature-dependent behavior and/or the presence of impurities allows researchers to optimize the synthesis and electronic conductivity.

3.0. Current Methods for Measuring Electronic Conductivity

In order to quantify the electronic properties of the 1D nanowires, conductivity measurements must be carried out. Measurements with two-point probes and four-point probes can be completed with the aid of a suitable substrate with custom designed probes and patterns that provide accuracy on small scales and the ability to assemble the materials into thin films for solid state measurements. Four-point probe measurements differ from two-point probe ones in that the former use different pairs of electrodes for current carrying and voltage sensing resulting in more accurate measurements. The small dimensions of the

materials being considered for these studies require the accuracy provided by four-point measurements, however a supportive substrate that allows control and precision over the deposition of the materials is still necessary.

Current methods include the functionalization of the substrate and micro- or nanocrystal surfaces with ligands that allow for interactions between the two^[49]. This functionalization can be accomplished by manipulating the photo-properties^{[50] [51]} of the ligands to create patterns of the material to be studied. Another method is to manipulate the substrate surface hydrophobicity in comparison to that of the desired material^[52]. By controlling the deposition of the thin film, the area to be measured is smaller, defects in the film are minimized, film evenness increases, fewer cracks form, and contact with probes is more likely.

Other techniques rely on physical concepts instead of the surface chemistry of the materials and are more suitable for studying the intrinsic electrical properties of micro- or nanocrystals. The use of etchants to create micro scale trenches is often utilized since control over the trench dimensions and the capillary forces acting on the crystals makes it an ideal method for precise placement of the material^[53]. A series of printing^{[54] [55]} and stamping techniques have also been extensively explored for the development of nano- and micro-patterned substrates and thin film measurements, however further functionalization and surface chemistry modification must be done to assure adhesion and compatibility^[54]. For precise conductivity measurements on the

nanometer scale, electron beam lithography and lift off processes^[56] have been demonstrated to work best. Results show position precision and dimensions ~30 nm and measurement accuracy 180 times higher than drop casting techniques^[56]. Therefore this method could be useful for our purposes, however the pattern must be customized for each material to be measured, which makes it cumbersome for screening a wide series of 1D nanowires.

There are examples of reusable four-point probe devices for a variety of micro crystals in which Au wires are incorporated into a substrate^[40] with fixed dimensions according to the design of the four point probe tips. Our approach is to use micro-fabrication techniques to develop a customized mask with micro probe extensions for accuracy and control of material deposition and ease of data collection.

4.0. Four-Point Probe Theory

A four-point probe apparatus allows us to determine bulk resistivity (and hence conductivity) of a material in which the mobility of the carriers is dependent on the impurities present in the lattice, the crystals defect density, and the temperature at which the measurements are carried out^[57]. The instrument consists of four colinear tungsten wire probes that are then positioned on the sample surface until contact is achieved as demonstrated in Figure 2.3. Figure 2.4. shows the instrument aligned on developed four point probe device. The four

thin probes allow current to flow between the two outer probes while the voltage is measured between the two inner probes with equal inter-probe spacing ($S=S_1=S_2=S_3$)^[58] (as shown in Figure 2.1. and Figure 2.4.). The resistivity of a semi-infinite volume is given by $\rho=(2)(\pi)(S)(V/I)$ in which rho represents the resistivity (ohms.cm), **S** the inter-probe spacing (cm), **V** the voltage (volt) and **I** the current (ampere)^[58]. The separation of the current carrying and voltage sensing electrodes eliminates the impedance contribution of the electrical leads and contact resistance resulting in increased measurement accuracy.

During the measurements, the current carrying electrodes generate a voltage drop (resistance) across the impedance that is measured by Ohm's Law $V=RI$, in which **V** is the voltage (volts), **R** is the resistivity (ohms) and **I** the current (ampere)^[58]. Subsequently, slight current goes through the sense electrodes and the voltage drop is extremely small.

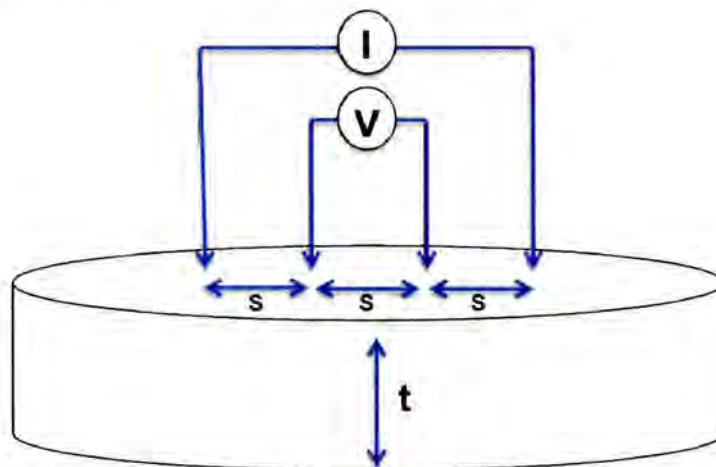


Figure 2.3. Four-point Probe system

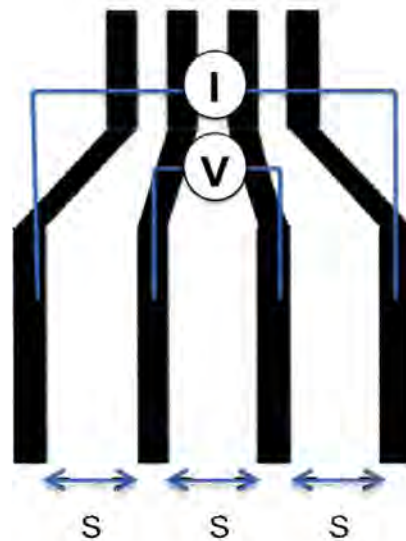


Figure 2.4. Four point probe device aligned to instrument with single inter-probe spacing (S)

5.0. Microfabrication Techniques

Micromachining

The exciting field of nanotechnology cannot be characterized or understood without the aid of micro scale measuring structures to bridge the gap to the macroscopic domain. Micromachining techniques allow us to develop the structures necessary to make that jump. Today, a wide variety of micromachining processes are utilized in industrial applications. For example, accelerometers small enough to be incorporated into portable technologies (phones, video games) for position detection by identifying the acceleration experienced by change in directional weight applied on the device are developed by

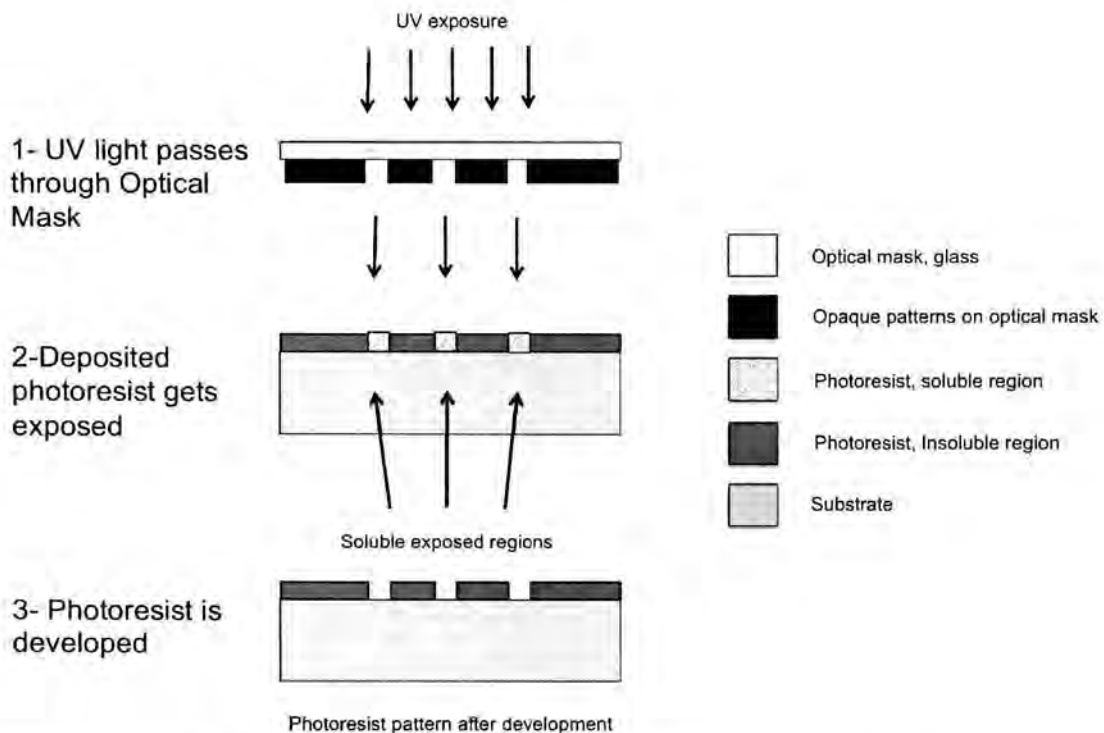
micromachining techniques using MEMS (Microelectromechanical systems)^[59] technology. Resistors^[60] and actuators^[61] are other examples. The top-down approach to micromachining processes in which bulk materials are shaped into microstructures allows flexibility and creativity in design development of the aforementioned structures. There are two distinguishable routes to micromachining: (i) bulk micromachining, in which materials are removed or etched from the bulk to achieve a 3-dimensional shape, and (ii) surface micromachining, in which the desired features are built upon the surface of a chosen substrate.

5.1. Surface micromachining

Unlike bulk micromachining, which relies heavily on etching techniques to define the structure, surface micromachining utilizes deposition techniques to define the structures and wet etching to release deposited materials from the substrate by undercutting. A general surface micromachining process consists of deposition of a patterned sacrificial layer onto the substrate followed by a structural layer. Subsequently, the structural layer is released by selective etching. Some of the advantages of this approach include freedom in design development and the ability to work with thin films, which is ideal for our measurement purposes.

5.2. Photolithography

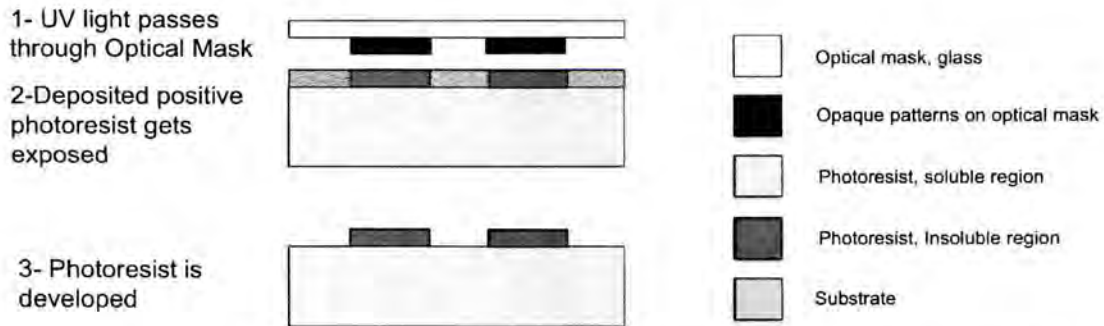
Lithography is a common process to pattern and define features on a substrate by spin-coating thin films of a photosensitive polymer layer on the substrate. Generally the coating is baked at $\sim 100^{\circ}\text{C}$ to harden the resist and remove residual solvents. An optical mask with the desired pattern featuring clear and opaque regions then selectively transmits and blocks UV light, resulting in the exposure of the unprotected photoresist areas (clear areas) of the mask, as depicted in Scheme 2.5. Exposure to UV light changes the chemistry of the photoresist, depending on the type of resist utilized, the result will be lower or higher solubility of the exposed areas, termed *positive* and *negative* photoresist.



Scheme 2.5. Lithography process by steps: 1) Optical Mask and UV exposure 2) exposure of photoresist coated substrate and pattern transfer 3) photoresist development

5.2.1. Positive Photoresist

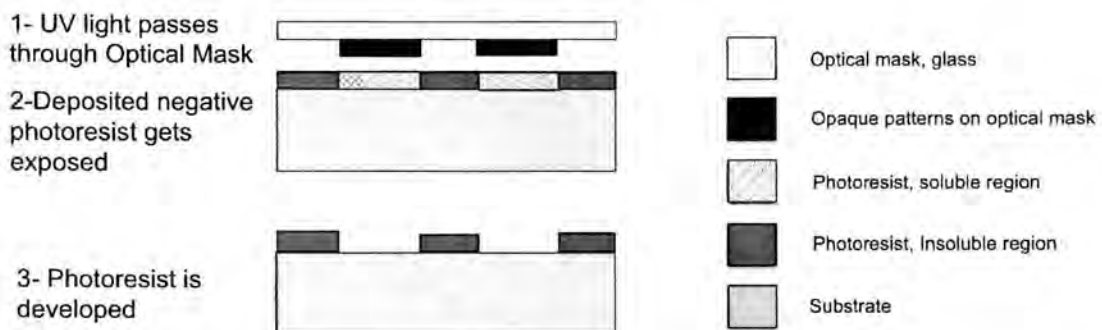
The regions exposed to UV light become cross-linked and, as a result, are insoluble in the developer solution as demonstrated in Scheme 2.6. Diazo photoactive compounds such as diazoquinone^[62], are often utilized in these positive photoresist systems such as S1818, where N_2 is weakly bonded and can be freed from the carbon ring upon UV exposure^[62].



Scheme 2.6. Photoresist pattern resulting from positive photoresist

5.2.2. Negative Photoresist

The regions exposed to UV light have their bonds broken and, as a result, are soluble in the developer solution as demonstrated in Scheme 2.7. A common example would be SU-8, an epoxy-based photoresist with an ability to spread a coating with a thickness between 1-300 μL ^[63]. During exposure to UV-light (365 nm) the long molecular chains of the epoxy cross link resulting in a stronger material.^[63]



Scheme 2.7. Photoresist pattern resulting from use of negative photoresist

6.0. General Procedures

The instruments utilized in this thesis are located in the Class 100 cleanroom (photolithography room) at the Boston University Photonics Center. Photoresist films were developed by use of a Headway Research photoresist spinner with a programmable controller as well as a flat top wet bench used for soft bakes, developing, and photoresist stripping/wafer cleaning. The optical mask pattern was produced by use of a DWL66 mask writer followed by development. The mask pattern was transferred onto the substrate by UV exposure with the Suss Microtech MJB3 and MA6 aligner. The chromium and gold layers were thermally evaporated by use of an Edwards Auto 306 Turbo thermal evaporator. The conductivity measurements were conducted by use of Cascade Microtech CPS-05 four-point Probe, which can test a variety of sample types, shapes and resistances, by adjustable control over tip pressure, choice of tip material, radii, and spacing. For our measurements a tungsten tip with a 0.0018 cm radius and 0.127 cm spacing (S) was utilized.

6.1. Materials

All solvents, reagents and materials were used as received from commercial sources unless stated otherwise. TTF-TCNQ (tetrathiafulvalene tetracyanoquinodimethane)^[64] was synthesized and provided by Fred Baddour

from the Doerr Lab, Boston University. Substrates utilized for all measurements consisted of fused silica 100 nm in diameter, 500 nm thickness, and polished on both sides. A Kurt J. Lesker chrome-plated tungsten rod and 1 mm diameter gold wire were used for deposition of the thermally evaporated wires.

The optical mask substrate consisted of a 6x6 inch soda lime (SL) glass from Nanofilm coated with a low reflective chrome layer and a $10,000\pm 100$ Å thick Az1518 positive photoresist. For the sacrificial layer, a positive Microposit S1818 electronic grade photoresist was utilized and the common developer utilized throughout the micro-fabrication process was Microposit MF319.

7.0. Experimental

7.1. CAD

The overall design, shown in Figure 5, was developed with AutoCad 2013 software and consisted of four adjacent columns 250 μm thick with 1270 μm spacing. The spacing decreased after a length of 6500 μm to a thickness of 1.0 μm and a column spacing of 5.0 μm with a total length of 10500 μm (Figure 2.5.). The file containing the design was saved as a .dxf file and transferred to the mask writer to proceed.

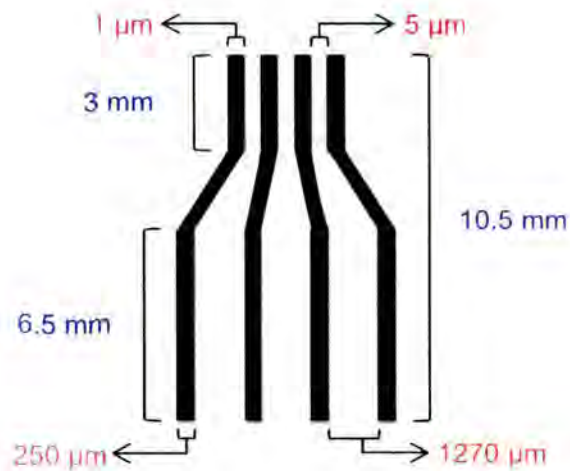


Figure 2.5. Mask design with micro features dimensions

7.2. Optical Mask

The glass substrate coated with a thin layer of positive photoresist (Az1518) was exposed to UV light under the mask writer, increasing the solubility of the exposed areas as shown in Scheme 2.5. step 1. Subsequently, the mask was submerged in ~500 mL of developer solution (MF 319) for 1 minute dissolving the exposed photoresist and immersed in running water for 30 seconds to wash off the residue. Once cleaned and dried, the mask is ready for further use.

7.3. Chromium Etch

A chromium layer also protects the glass substrate that, after UV exposure and resist development, is also etched. It is necessary to develop the clear regions of the chromium layer to obtain a high contrast and better transparency. This effect was achieved by submerging the mask into ~100 mL of chromium etchant, which consists of an aqueous solution of ammonium nitrate and nitric acid, for 1 minute and then in running water for ~30 seconds to wash off any residue. The optical mask developed with the dimensions depicted in Figure 2.5. was then cleaned and dried. The final optical mask is shown in Figures 6 and 7. A detail of the bottom region of the pattern is depicted on Figure 2.8.

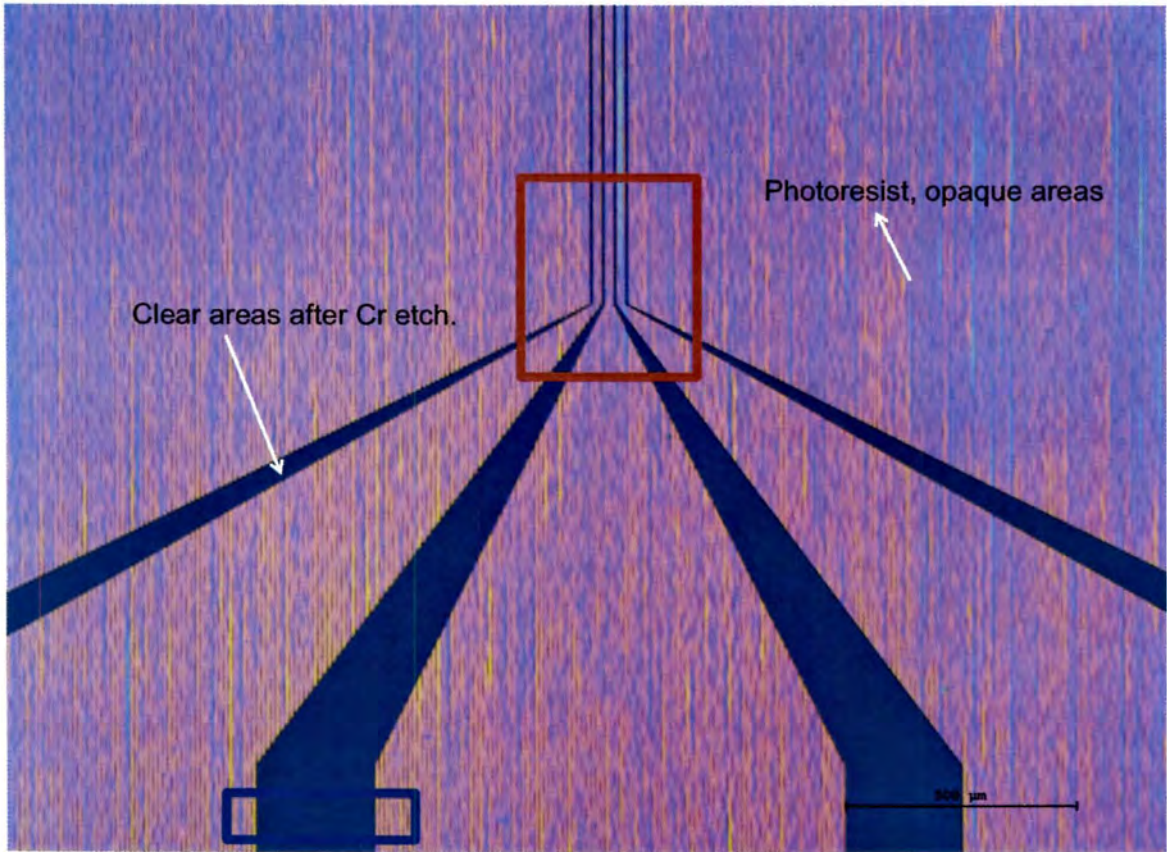


Figure 2.6. Detail of developed optical mask, (red box: Figure 2.7., Blue box: Figure 2.8)

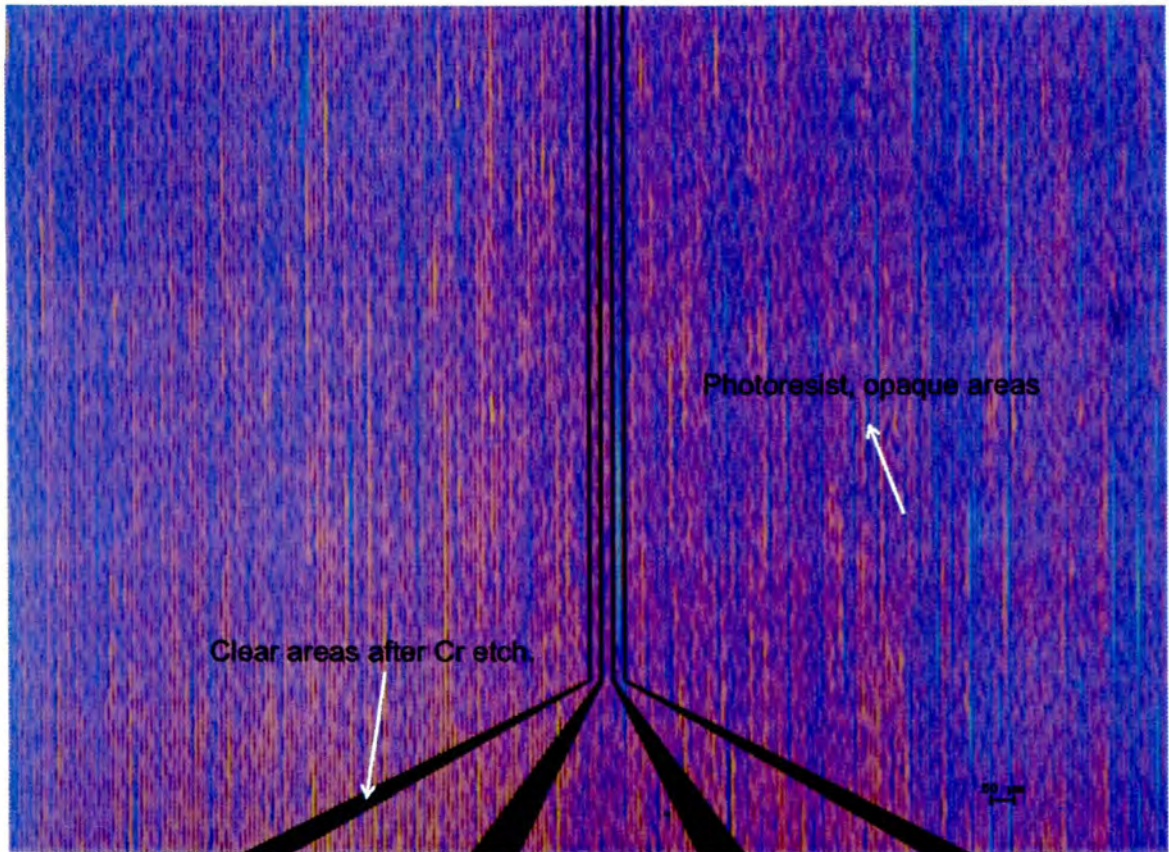


Figure 2.7. Detail of developed optical mask, close up of Figure 2.6. (red box on Figure 2.6.).

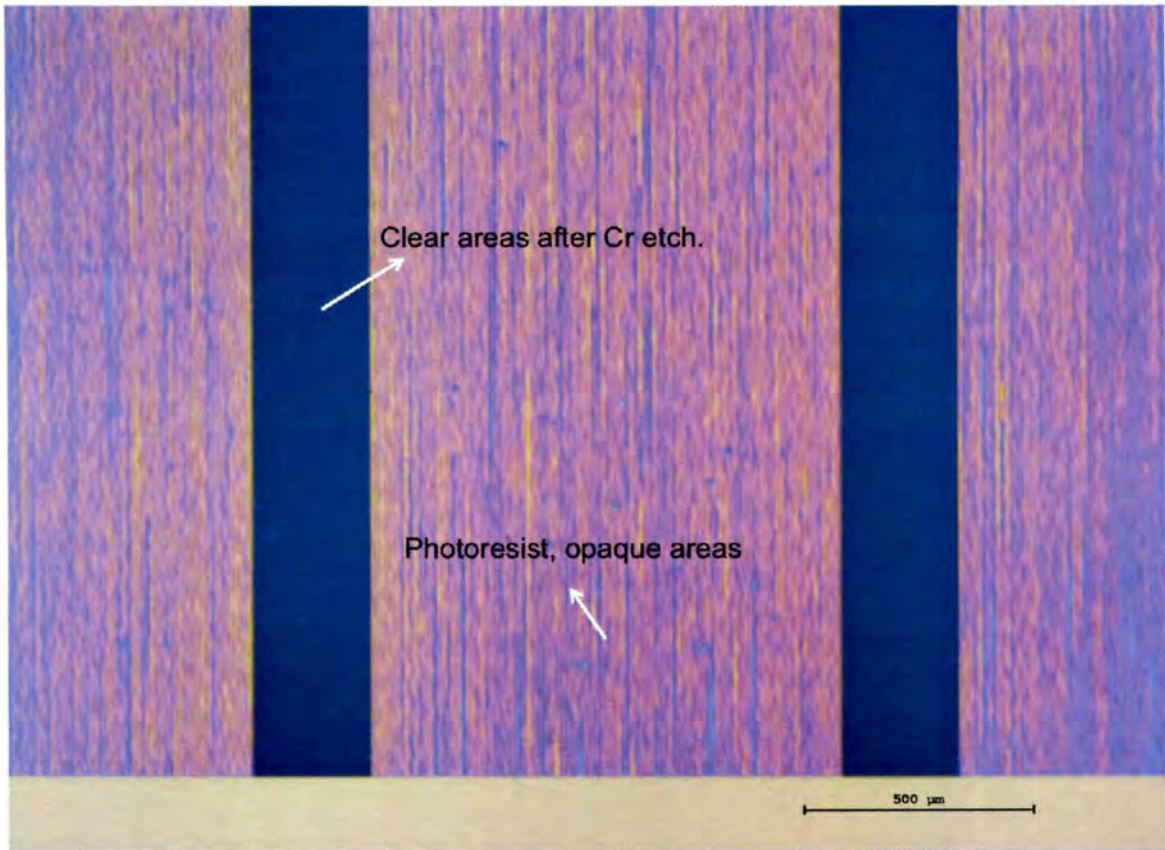


Figure 2.8. Detail of optical mask, close up from Figure 2.6., bottom region (blue box on Figure 2.6.)

7.4. Device Development

Fused silica was spin coated with a positive photoresist layer (SU1818) at 4000 rpm for 30 seconds to obtain a 1900 nm layer determined by a spin speed curve calibration from which a thickness is provided according to the revolutions per minute chosen in the settings. A thick enough layer allows for flexibility of the amount of metal deposition and protects the features. The resist mask was then

defined by “projection” lithography in which the optical mask was located above the photoresist surface followed by UV light exposure to transfer the pattern to the wafer as demonstrated in Scheme 2.5. step 2. Subsequently, the mask was submerged in 500 mL of developer solution (MF 319) for 1.5 minutes and then through running water for 30 seconds as demonstrated in Scheme 2.5. step 3. Once the substrate was cleaned and dried, the pattern’s features were evident on the substrate, as shown in Figure 2.9.

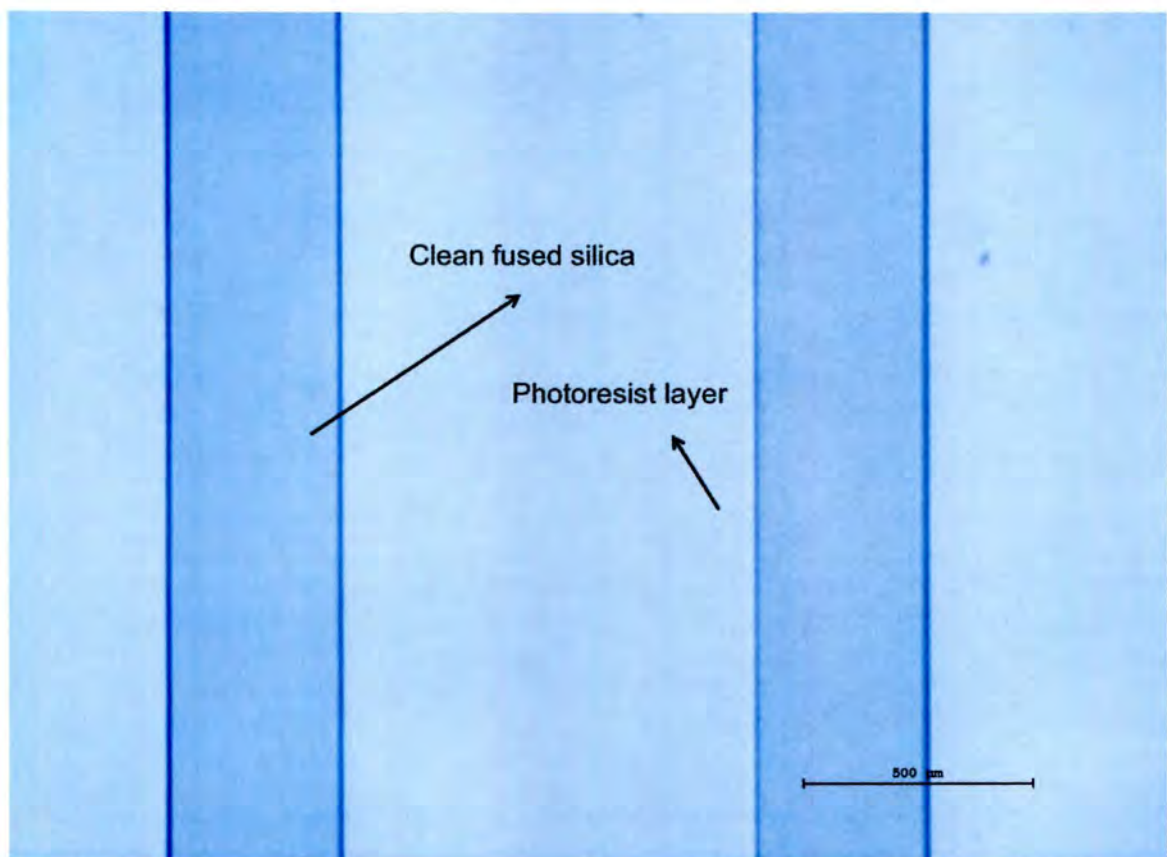


Figure 2.9. Fused silica substrate coated with photoresist after exposure and development (same region of the pattern as in Figure 2.8.)

7.5. Thermal Evaporation of Wires

In order to ensure Au adhesion to the silica surface, a chromium adhesion layer of 5 nm was thermally evaporated onto the patterned substrate, followed by a 95 nm gold layer. Once the evaporated material cooled to room temperature, it was submerged in 500 mL of acetone in order to remove the sacrificial layer (the photoresist) and sonicated for 5 minutes in order to obtain optimal results. A final picture of the overall device is shown in Figure 2.10., three different views of the same prototype are depicted. Details of final device are shown in Figures 2.12. and 2.11.



Figure 2.10. Picture of final product. Au wires deposited on fused silica with dimensions illustrated in Figure 2.5.

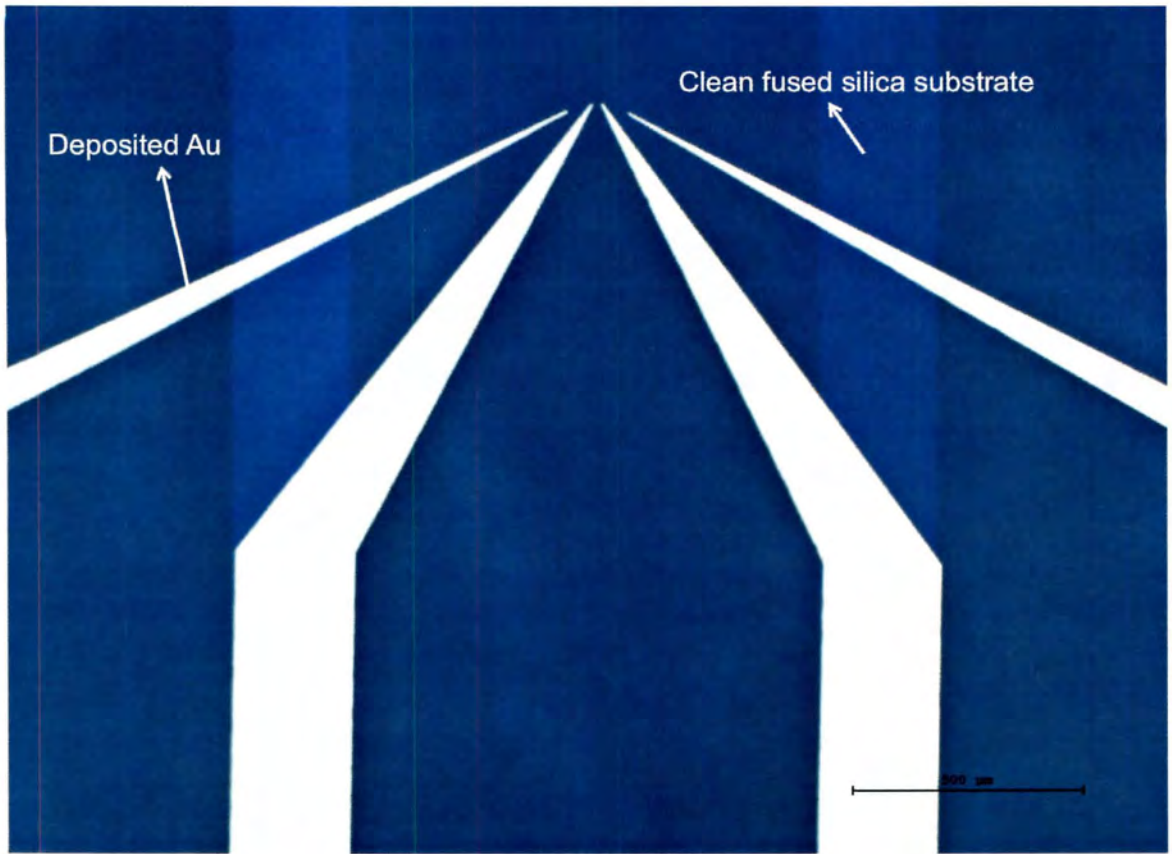


Figure 2.11. Au wires deposited on fused silica substrate

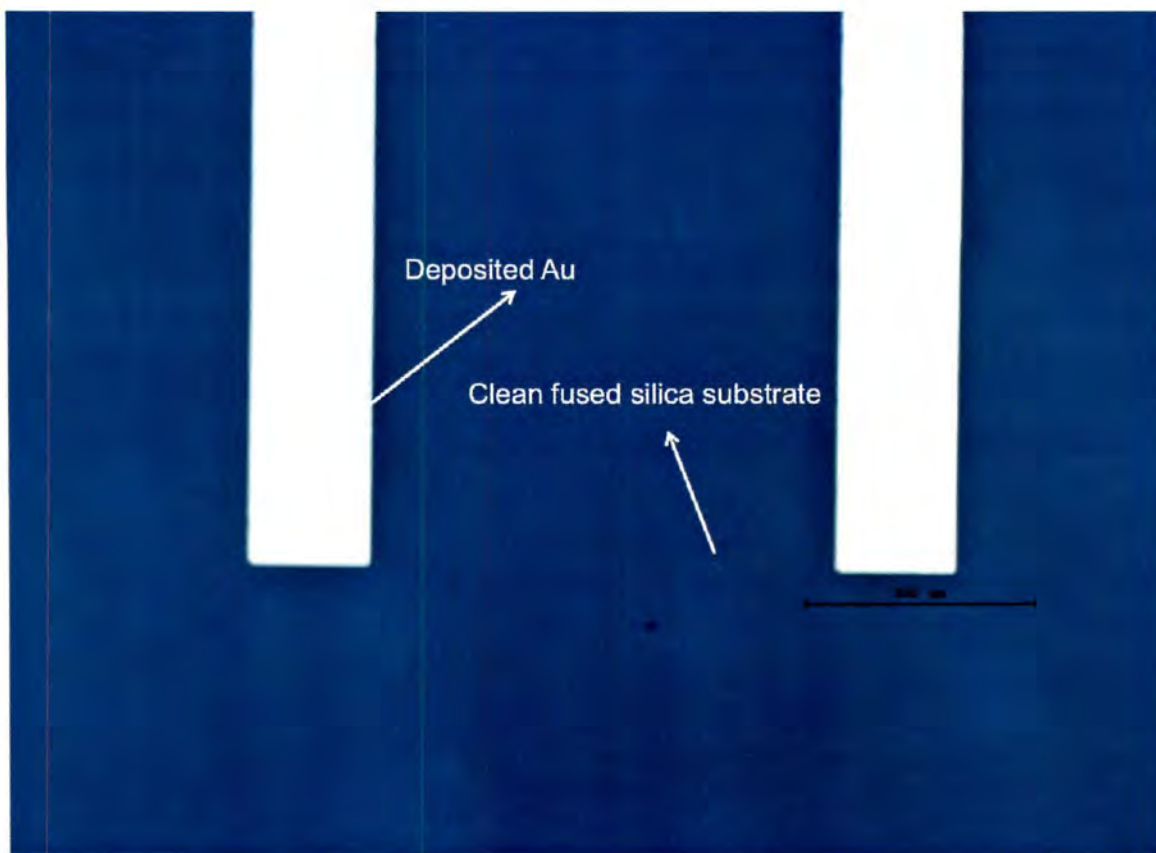


Figure 2.12. Detail of bottom region of Au wires deposited on fused silica

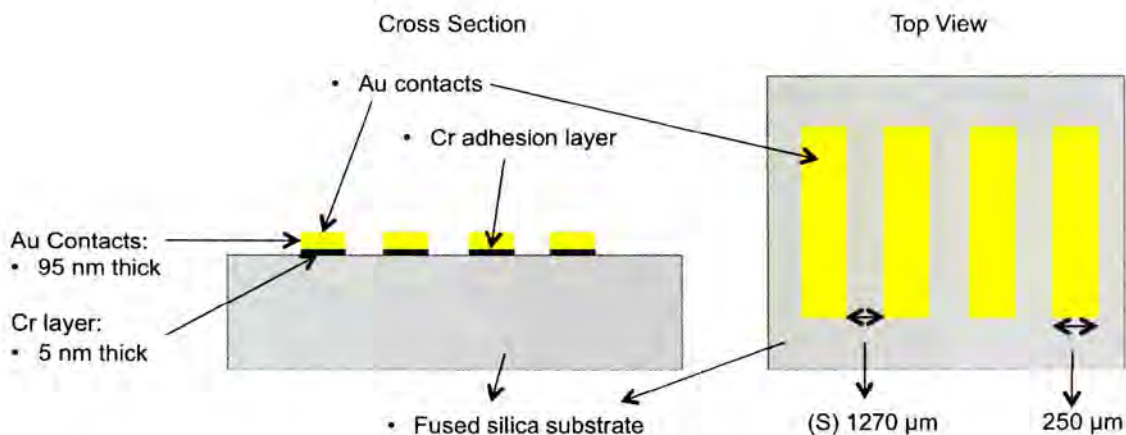
7.6. Four-point Probe Sample Preparation

All measurements were carried out at room temperature. A thin film of each sample was applied by 5 μL additions of a 10 mg/mL TTF-TCNQ/acetone solution, until enough contact with the electrodes was achieved. After each addition the solvent was left to evaporate to ensure the formation of a thin film. Resistivity measurements were then carried out for a TTF-TCNQ sample and repeated multiple times for precision. After the data were collected, the device

was submerged in acetone and sonicated for 1 min to thoroughly clean the reusable device.

8.0. Results and Discussion

The development of functional optical masks with different submicron features has been achieved for future use. Figure 2.5. illustrates the dimensions of the optical mask utilized for the device shown in Figure 2.10. Difficulties during the deposition of the Cr and Au layer suggested that the dimensions of the submicron features were not suitable for the deposition process. The rest of the pattern was deposited with Cr and Au successfully with precise definition as demonstrated in the macroscopic Figure 2.10 in which the deposited Au wires are shown and the details of Figures 2.11 and 2.12. The prepared substrate is suitable for use as described in Section 7.6 since probes accurately line up with the four point probe chosen tip as illustrated in Figure 2.4. The final prototype is illustrated in detail in Scheme 2.8. both in a cross section view (left) for the materials and a top view (right) for the dimensions.



Scheme 2.8. Illustration of final device with depiction of materials and dimensions

8.1. Measurements

In order to test the accuracy of our device, an extensively studied material has been chosen as a control. TTF-TCNQ (tetrathiafulvalene tetracyanoquinodimethane) is a donor-acceptor organic molecule in which π ... π interactions lead to the formation of narrow band and an anisotropic semiconducting material^{[65] [66] [67] [68]}.

Resistivity data were collected after three 5 μ L additions of a 10 mg/mL TTF-TCNQ/acetone solution drop-casted directly on the device for best results. Readings of sheet resistivity range between 1.92-92.0 K Ω at room temperature as demonstrated on Table 2.1. These data concur with published results with similar parameters (<100 K Ω)^{[65] [66] [67] [68]}, which is promising for our desired

measurements of the aforementioned 1(D) nanowires. The developed device has also proven to be robust enough for reuse and ease of cleaning makes it ideal for multiple uses in short time frame.

Table 2.1. Resistivity Measurements

μL of solution	Resistivity ($\text{k}\Omega$)
5	1.92
15	64.7
25	79.5
35	92.0

8.2. Further Optimization

Further optimization of the original dimensions for the optical mask must be undertaken since the use of features $<1\ \mu\text{m}$ were found to push the resolution limits of the thermal evaporator during the deposition of Cr and Au. A new approach led us to increase the size of the sub-micron probes up to $5\ \mu\text{m}$ in order obtain better definition in this region of the pattern during the photoresist development. The new design is depicted in Figure 2.13. in which a pattern with the smallest feature of $5\ \mu\text{m}$ is illustrated. During the pattern transfer by UV light exposure, the development of $1\ \mu\text{m}$ features was challenging. Increments of 10 seconds were added to original developing time to improve the pattern definition.

Results were underdeveloped for the smallest features, however, overdevelopment throughout the rest of the structure started to be evident as shown in Figure 2.14.

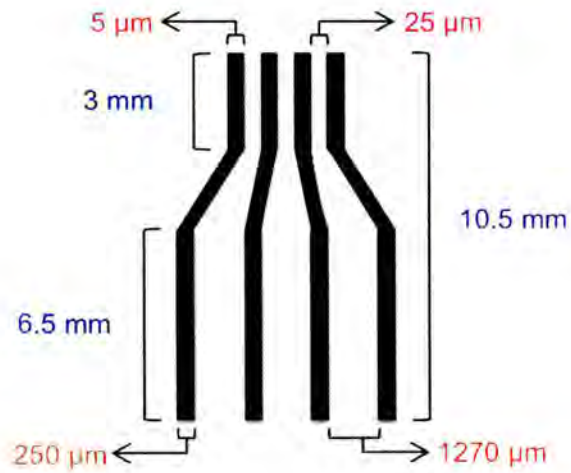


Figure 2.13. Illustrations of new dimensions for optical mask with smallest feature of 5μm

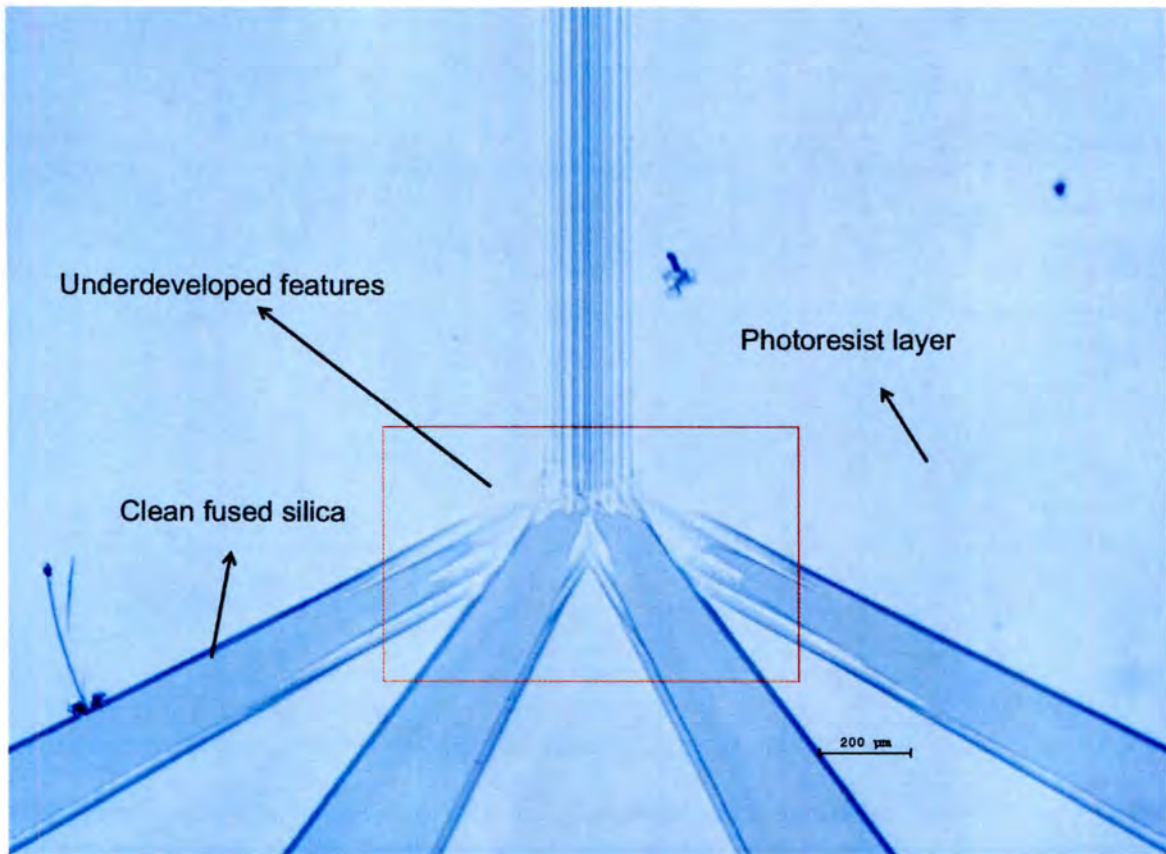
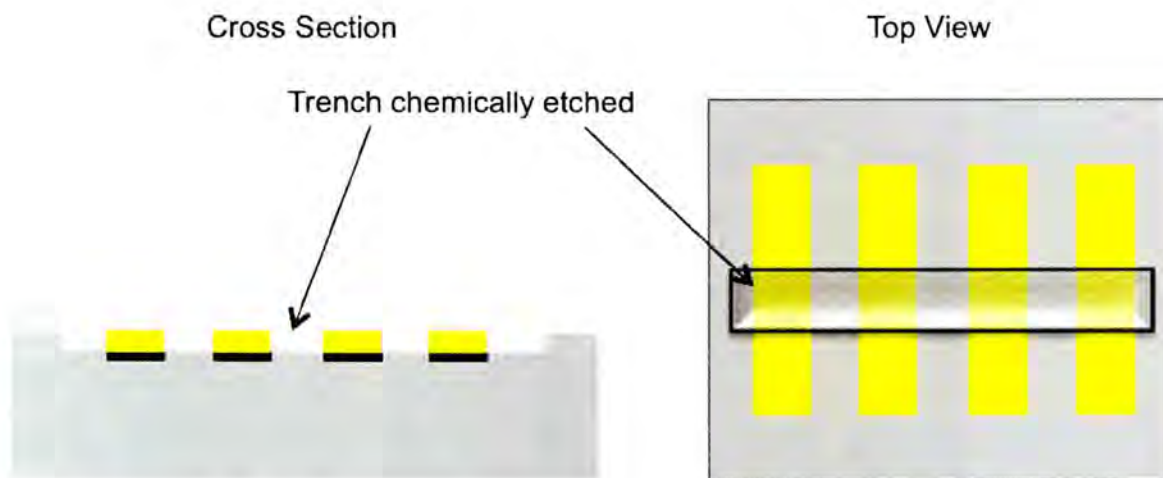


Figure 2.14. Unsuccessful development of pattern on photoresist coated fused silica

After successful development of the optical mask with sub-micron features of 5 μm shown in Figure 2.12., structure definition was improved, however during thermal evaporation no deposition was achieved in the patterned submicron probes. Alignment of the mask can still be improved utilizing the aforementioned optical mask as well as further optimization of the development time.

8.3. Future Development- A New Approach

To avoid cracks and defects in the thin films to be measured by a four point probe, instead of drop-casting the sample, microcrystals could be formed directly on the device by chemically etching a trench of specific area that was also deposited with Cr and Au wires as shown in Scheme 2.9. The pattern would be the same as described previously in this chapter (section 7) however a trench would be developed in the center of the substrate to provide a container for slow evaporation of a solution of the sample, which could potentially result in crack-free crystalline films.



Scheme 2.9. Illustration of device introducing a trench for slow evaporation

9.0. Summary and Conclusion

Utilizing proven micromachining techniques, a device for four point probe measurements has been achieved with Au deposited wires compatible with a four point probe instrument. This device provides reliable data as demonstrated in the resistivity measurements of TTF-TCNQ thin films. The proposed sub-micron features proved challenging to resolve on a scale $<1 \mu\text{m}$, however the development of an optical mask featuring a pattern with probes $5 \mu\text{m}$ wide is a promising new direction in order to obtain the desired design. Another approach to improvement of the device is the introduction of a chemically etched trench for slow evaporation of 1D nanowires in order to avoid lattice defects in the film formation.

Preliminary design and development results of the four point probe device have opened an exciting path for resistivity characterization of 1D nanowires. Obtaining resistivity and conductivity data for the series of 1D nanowires currently synthesized and otherwise characterized^[34] could shape the direction of the synthesis and optimization of the aforementioned materials as well as their classification according to electronic properties.

References

- [1] a) P. Sivakumar, R. Ramesh, A. Ramanand, S. Ponnusamy and C. Muthamizhchelvan, *Materials Research Bulletin* **2011**, *46*, 2208-2211; b) B. Baruwati, M. N. Nadagouda and R. S. Varma, *Journal of Physical Chemistry C* **2008**, *112*, 18399-18404; c) C.-F. Leung Ken and J. W. Yi-Xiang in *Mn-Fe Nanowires Towards Cell Labeling and Magnetic Resonance Imaging*, Vol. **2010**; d) M. Bellusci, S. Canepari, G. Ennas, B. A. La, F. Padella, A. Santini, A. Scano, L. Seralessandri and F. Varsano, *Journal of the American Ceramic Society* **2007**, *90*, 3977-3983; e) G.-h. Ren and Z.-s. Yu, *Diffusion and Defect Data, Pt. B* **2012**, *181-182*, 393-396.
- [2] a) E. J. Choi, Y. Ahn and Y. D. Her, *Journal of th Korean Physics Society*. **2007**, *50*, 460-463; b) S. Briceno, Y. Sanchez, W. Bramer-Escamilla, P. Silva, J. P. Rodriguez, M. A. Ramos and E. Plaza, *Acta Microscopica* **2013**, *22*, 62-68.
- [3] P. S. Silinsky and M. S. Seehra, *Physical Review B* **1981**, *24*, 419-423.
- [4] a) A. Ito, M. Shinkai, H. Honda and T. Kobayashi, *J. Biosci. Bioeng.* **2005**, *100*, 1-11; b) X. Wang and L. Nie, *Huaxue Tongbao* **2009**, *72*, 489-494.
- [5] P. K. Sharma, R. K. Dutta and A. C. Pandey, *Advance Materials Letters* **2011**, *2*, 246-263.
- [6] a) X. Jin, Y. Li and H. Li in *Method for synthesis and purification of hydrogen from natural gas by catalytic desulfurization and reforming*, Vol. Suzhou Jinhong Gas Co., Ltd., Peop. Rep. China . **2013**, p. 6pp; b) M. S. Lee, J. Y. Lee, D.-W. Lee, D. J. Moon and K.-Y. Lee, *International Journal of Hydrogen Energy* **2012**, *37*, 11218-11226; c) L. S. Neiva, A. N. Simoes, A. C. F. M. Costa, H. M. C. Andrade, M. R. Quirino and L. Gama, **2011**, pp. 403-406.
- [7] P. Tang and N. Liu, *Dongbei Nongye Daxue Xuebao* **2007**, *38*, 420-423.
- [8] R. Valenzuela, *Physics Research International* **2012**, 591839, 591839 pp.
- [9] R. Valenzuela, *Magnetic Ceramics. [In: Chemistry of Solid State Materials, 1994; 4]*, Cambridge Univ. Press, **1994**, p. 312 pp.
- [10] D. S. Mathew and R.-S. Juang, *Chemical Engineering Journal* **2007**, *129*, 51-65.
- [11] F. J. Owens, C. P. Poole, Jr. and Editors, *The Physics and Chemistry of Nanosolids*, John Wiley & Sons, Inc., **2008**, p. 539 pp.

- [12] a) B. Smith and J. A. Nason, **2013**, pp. ENVR-261; b) X. Wang, J. Stoeber, V. Zielasek, L. Altmann, K. Thiel, K. Al-Shamery, M. Bauemer, H. Borchert, J. Parisi and J. Kolny-Olesiak, *Langmuir* **2011**, 27, 11052-11061; c) M. Michno and K. Bandyopadhyay, **2013**, pp. CHED-877.
- [13] J. Salafranca, J. Gazquez, N. Perez, A. Labarta, S. T. Pantelides, S. J. Pennycook, X. Batlle and M. Varela, *Nano Letters*. **2012**, 12, 2499-2503.
- [14] U. Schwertmann and R. M. Cornell, *Iron Oxides in the Laboratory, 2nd Edition*, John Wiley & Sons, Ltd., **2000**, p. 154 pp.
- [15] K. H. J. Buschow and F. R. de Boer, *Physics of Magnetism and Magnetic Materials*, Springer, **2003**, p.
- [16] W. Shumann, *Gemstones of the World 3rd edition*, Sterling, **2006**, p.
- [17] T.-J. Li, C.-C. Huang, D.-B. Shieh and C. S. Yeh, **2012**, pp. 757-758.
- [18] W. H. Bragg, *Philosophical Magazine (1798-1977)* **1915**, 30, 305-315.
- [19] a) C. Cannas and D. Peddis, *Chimica e Industria. (Milan, Italy)* **2012**, 94, 109-117; b) Y. Yafet and C. Kittel, *Physics Reviews* **1952**, 87, 290-294.
- [20] a) S.-S. Chee and J.-H. Lee, *transactions of Nonferrous Metals Society China* **2012**, 22, s707-s711; b) S. F. Hasany, A. Rehman, R. Jose and I. Ahmed, *AIP Conference Proceedings*. **2012**, 1502, 298-321; c) J.-P. Jolivet, M. Henry, J. Livage and E. Bescher, *Metal Oxide Chemistry and Synthesis: From Solution to Solid State*, John Wiley & Sons, Ltd., **2000**, p. No pp. given; d) P. M. Kutty, S. Dasgupta and S. Bandyopadhyay, *Material Science of Polymers*. **2011**, 29, 121-126; e) W. W. Yu, J. C. Falkner, C. T. Yavuz and V. L. Colvin, *Chemical Communications. (Cambridge, U. K.)* **2004**, 2306-2307.
- [21] a) M. V. Kuznetsov, Y. G. Morozov and O. V. Belousova, *Inorganic Materials*. **2012**, 48, 1044-1051; b) K. Gheisari, S. Shahriari and S. Javadpour, *Journal of Alloys Compounds*. **2013**, 552, 146-151; c) T. F. Marinca, I. Chicinas, O. Isnard and V. Popescu, *Journal of the American Ceramic Society*. **2013**, 96, 469-475; d) M. Kakazey, M. Vlasova, M. Dominguez-Patino, E. A. Juarez-Arellano, A. Bykov, I. Leon and A. Siqueiros-Diaz, *Journal of Magnetism and Magnetic Materials*. **2011**, 323, 2429-2435.
- [22] a) U. F. Aghayeva, M. P. Nikitin, S. V. Lukash and S. M. Deyev, *ACS Nano* **2013**, 7, 950-961; b) Y. Yuan, S. Zhang and W. You, *Journal of Sol-Gel Science and Technology*. **2004**, 30, 223-227.

- [23] L.-h. Shen, J.-f. Bao, D. Wang, Y.-x. Wang, Z.-w. Chen, L. Ren, X. Zhou, X.-b. Ke, M. Chen and A.-q. Yang, *Nanoscale* **2013**, *5*, 2133-2141.
- [24] S. S. Kang, S. T. Ahn and D. N. Yoon, *Metallography* **1981**, *14*, 267-270.
- [25] A.-H. Lu, E. L. Salabas and F. Schüth, *Angewandte Chemie International Edition* **2007**, *46*, 1222-1244.
- [26] A. Tavakoli, M. Sohrabi and A. Kargari, *Chemical Papers*. **2007**, *61*, 151-170.
- [27] a) A. Sutka, G. Mezinskis, A. Pludons and S. Lagzdina, *Energetika (Vilnius, Lith.)* **2010**, *56*, 254-259; b) H. Arabi and F. Ganjali, *Journal of Superconductivity and Novel Magnetism*. **2013**, *26*, 1031-1035.
- [28] R. Guo, L. Fang, W. Dong, F. Zheng and M. Shen, *Journal of Materials Chemistry*. **2011**, *21*, 18645-18652.
- [29] a) H. Liu, Y. Chen, S. Pei, G. Liu and J. Liu, *Journal of Sol-Gel Science and Technology*. **2013**, *65*, 443-451; b) M. Saif, *Journal of Luminescence*. **2013**, *135*, 187-195.
- [30] a) C. Pecharroman, T. Gonzalez-Carreno and J. E. Iglesias, *Physics and Chemistry of Minerals*. **1995**, *22*, 21-29; b) P. Tartaj, M. d. P. Morales, S. Veintemillas-Verdaguer, T. Gonzalez-Carreno and C. J. Serna, *Journal of Physics. D: Applied Physics*. **2003**, *36*, R182-R197; c) T. Maeda, M. Nagasawa, K. Sogabe and T. Kato in *Ferrous metal nitride films and method and apparatus for their formation by aerosol deposition*, Vol. Sumitomo Electric Industries, Ltd., Japan . **2013**, p. 13pp.
- [31] A. Vashist, S. Shahabuddin, Y. K. Gupta and S. Ahmad, *Journal of Materials Chemistry B* **2013**, *1*, 168-178.
- [32] L. Perez-Mirabet, E. Solano, F. Martinez-Julian, R. Guzman, J. Arbiol, T. Puig, X. Obradors, A. Pomar, R. Yanez, J. Ros and S. Ricart, *Materials Research Bulletin*. Ahead of Print.
- [33] S.-Y. Fu and X.-M. Liu, **2007**, pp. 165-204.
- [34] F. G. Baddour in *Platinum-Containing Heterobimetallic Lantern Complexes Prepared With Thiocarboxylates: Synthesis, Structural, And Magnetic Characterization And Synthesis And Characterization of Magnetic Metal Oxide Nanoparticles*, Vol. Doctor of Philosophy Boston University, **2013**.

- [35] M. Diskus, O. Nilsen and H. Fjellvåg, *Chemical Vapor Deposition* **2011**, *17*, 135-140.
- [36] K. K. Bharathi, K. Balamurugan, P. N. Santhosh, M. Pattabiraman and G. Markandeyulu, *Physics Review B: Condense Matter and Materials, Physics*. **2008**, *77*, 172401/172401-172401/172404.
- [37] K. Rajeshwar and F. Roozeboom, *Electrochemical Society Interface* **2007**, *16*, 11.
- [38] G. Magnus, *Ann. Chim. Phys. Sér.* **1829**, *40*.
- [39] J. S. Miller and A. J. Epstein, *Progress in Inorganic Chemistry*. **1976**, *20*, 1-151.
- [40] M. G. Campbell, D. C. Powers, J. Raynaud, M. J. Graham, P. Xie, E. Lee and T. Ritter, *Nature Chemistry*. **2011**, *3*, 949-953.
- [41] L. H. Doerrer, *Dalton transstions*. **2010**, *39*, 3543-3553.
- [42] F. A. Cotton, C. A. Murillo and R. A. Walton, *Multiple Bonds Between Metal Atoms*, Springer, **2005**, p.
- [43] E. W. Dahl, F. G. Baddour, S. R. Fiedler, W. A. Hoffert, M. P. Shores, G. T. Yee, J.-P. Djukic, J. W. Bacon, A. L. Rheingold and L. H. Doerrer, *Chemical Science*. **2012**, *3*, 602-609.
- [44] V. Phillips, K. J. Willard, J. A. Golen, C. J. Moore, A. L. Rheingold and L. H. Doerrer, *Inorganic Chemistry*. **2010**, *49*, 9265-9274.
- [45] G. R. Newkome, V. K. Gupta and F. R. Fronczek, *Organometallics* **1982**, *1*, 907-910.
- [46] S. Takamizawa, E.-i. Nataka, T. Akatsuka, R. Miyake, Y. Kakizaki, H. Takeuchi, G. Maruta and S. Takeda, *Journal of the American Chemical Society*. **2010**, *132*, 3783-3792.
- [47] F. G. Baddour in *Manuscript in preparation*, Vol. **2013**.
- [48] C. Kittel, *Introduction to Solid State Physics. 5th Ed*, Oldenbourg, **1980**, p. 640 pp.
- [49] T. Tsuruoka, K. Akamatsu and H. Nawafune, *Langmuir* **2004**, *20*, 11169-11174.

- [50] C. Lu, N. Wu, F. Wei, X. Zhao, X. Jiao, J. Xu, C. Luo and W. Cao, *Advance Functional Materials*. **2003**, 13, 548-552.
- [51] J.-J. Park, P. Prabhakaran, K. K. Jang, Y. G. Lee, J. Lee, K. H. Lee, J. Hur, J.-M. Kim, N. Cho, Y. Son, D.-Y. Yang and K.-S. Lee, *Nano Letters*. **2010**, 10, 2310-2317.
- [52] a) J. Aizenberg and S. Yang in *Process for making reversibly adaptive rough micro- and nano-structures*, Vol. Lucent Technologies, USA; The Trustees of the University of Pennsylvania . **2006**, p. 14 pp; b) B. Hatton, L. Mishchenko, J. Aizenberg, T. Krupenkin and A. J. Taylor in *Patterned superhydrophobic surfaces to reduce ice formation, adhesion, and accretion*, Vol. Harvard College, USA; Wisconsin Alumni Research Foundation . **2011**, p. 33pp.
- [53] Y. Cui, M. T. Bjoerk, J. A. Liddle, C. Soennichsen, B. Boussert and A. P. Alivisatos, *Nano Letters*. **2004**, 4, 1093-1098.
- [54] M. J. Hampton, J. L. Templeton and J. M. DeSimone, *Langmuir* **2010**, 26, 3012-3015.
- [55] E. Tekin, P. J. Smith, S. Hoepfner, d. B. A. M. J. van, A. S. Susha, A. L. Rogach, J. Feldmann and U. S. Schubert, *Advance Functional Materials*. **2007**, 17, 23-28.
- [56] T. S. Mentzel, D. D. Wanger, N. Ray, B. J. Walker, D. Strasfeld, M. G. Bawendi and M. A. Kastner, *Nano Letters*. **2012**, 12, 4404-4408.
- [57] V. L. B., *Proceedings of the IRE* **1954**.
- [58] F. M. Smits, *BSTJ* **1958**, 37.
- [59] Z. Zhang, J. Wu, S. Bernard and R. G. Walmsley, *IEEE Electronic Components and Technology Conference*. **2012**, 62nd, 350-355.
- [60] a) S. Jung, A. Sou, E. Gili and H. Sirringhaus, *Organic Electronics*. **2013**, 14, 699-702; b) J. Woo, S. Kim, W. Lee, D. Lee, S. Park, G. Choi, E. Cha and H. Hwang, *Applied Physics Letters*. **2013**, 102, 122115/122111-122115/122114.
- [61] a) R. C. Gutierrez in *Surface mount mems actuator*, Vol. DigitalOptics Corporation MEMS, USA . **2013**, p. 30pp; b) R. C. Gutierrez, R. J. Calvet and A. Jain in *Multiple degree of freedom actuator*, Vol. Digitaloptics Corporation Mems, USA . **2013**.

- [62] M.-H. Cha, J.-H. Lee, M.-R. Im, M.-K. Chung, J.-Y. Jeong, H.-Y. Cho and H.-S. Cheon in *Positive photosensitive resin composition, photosensitive resin film prepared by using the same, and semiconductor device including the photosensitive resin film*, Vol. Cheil Industries Inc., S. Korea . **2012**, p. 24pp.
- [63] S. A. Ostrow, II and R. A. Coutu, Jr., *Journal of Micro/Nanolithography, MEMS, MOEMS* **2011**, 10, 033016/033011-033016/033017.
- [64] F. G. Baddour in *Unpublished Work*, Vol. **2013**.
- [65] H. D. Alves, A. S. Molinari, H. Xie and A. F. Morpurgo, *arXiv preprint arXiv:0810.0361* **2008**.
- [66] E. M. Engler, B. A. Scott, S. Etemad, T. Penney and V. V. Patel, *Journal of the American Chemical Society* **1977**, 99, 5909-5916.
- [67] A. J. Heeger and A. F. Garito in *The electronic properties of TTF-TCNQ*, Vol. 34 (Ed. H. G. Schuster), Springer Berlin Heidelberg, **1975**, pp. 151-183.
- [68] S. A. Odom, M. M. Caruso, A. D. Finke, A. M. Prokup, J. A. Ritchey, J. H. Leonard, S. R. White, N. R. Sottos and J. S. Moore, *Advanced Functional Materials* **2010**, 20, 1721-1727.

Curriculum Vitae

[REDACTED]

[REDACTED]

[REDACTED]

[REDACTED]

[REDACTED]

[REDACTED]

[REDACTED]

[REDACTED]

[REDACTED]

[REDACTED]

[REDACTED]

[REDACTED]

[REDACTED]

[REDACTED]

[REDACTED]

[REDACTED]